

An experimental study on deformation and failure mechanical behavior of granite containing a single fissure under different confining pressures

Sheng-Qi Yang¹ · Yan-Hua Huang¹

Received: 14 January 2017 / Accepted: 4 May 2017 / Published online: 13 May 2017
© Springer-Verlag Berlin Heidelberg 2017

Abstract Fissures in natural rocks play an important role in determining the strength, deformability and failure behavior of rock mass. However in the past, triaxial compression experiments have rarely been conducted for rock materials containing three-dimensional (3-D) fissures and the failure mechanical behavior of fissured rocks is not well known due to the difficulty of conducting triaxial experiments on fissured rocks. Therefore in this research, conventional triaxial compression experiments were performed to study the strength, deformability and failure behavior of granite specimens with one preexisting open fissure. Thirty-one specimens were prepared to perform conventional triaxial compression tests for intact and fissured granite. First, based on the experimental results, the effects of the confining pressure and the fissure angle on the elastic modulus and the peak axial strain of granite specimens are analyzed. Second, the influence of the confining pressure on the crack damage threshold and the peak strength of granite with respect to various fissure angles are evaluated. For the same fissure angle, the crack damage threshold and the peak strength of granite both increase with the confining pressure, which is in good agreement with the linear Mohr–Coulomb criterion. With increasing fissure angle, the cohesion of granite first increases and later decreases, but the internal friction angle is not obviously dependent on the fissure angle. Third, nine crack types are identified to analyze the failure characteristics of granite specimens

containing a single fissure under conventional triaxial compression. Finally, a series of X-ray microcomputed tomography (CT) observations were conducted to analyze the internal damage mechanism of granite specimens with respect to various fissure angles. Reconstructed 3-D CT images indicate obvious effects of confining pressure and fissure angle on the crack system of granite specimens. The study helps to elucidate the fundamental nature of rock failure under conventional triaxial compression.

Keywords Granite · Triaxial compression · Single fissure · Strength · Crack damage threshold · X-ray micro CT · Crack

Introduction

Fissures in natural rocks play an important role in determining the strength, deformability and failure behavior of rock masses (Wong and Chau 1998; Li et al. 2005; Prudencio and Van Sint Jan 2007; Park and Bobet 2009; Lee and Jeon 2011; Yang and Jing 2011; Yang et al. 2008, 2012a). Figure 1a illustrates a typical granite rock mass with a steep slope at the Three Gorges Project (TGP) located in Yichang city, Hubei province, China (modified after Shi 2006). It is clear that the granite rock mass developed by wedge failure due to the effect of two larger fissures. Therefore, it is significant to investigate the failure mechanical behavior of fissured rocks to assure the stability and safety of fissured rock slopes in such applications as high slope engineering and deep tunnel engineering.

The simplified geometry of a single fissure is often adopted to investigate the effect of fissure angle and fissure length on the failure mechanical behavior of all kinds of rock material (Fujii and Ishijima 2004; Lu et al. 2008;

✉ Sheng-Qi Yang
yangsqi@hotmail.com

¹ State Key Laboratory for Geomechanics and Deep Underground Engineering, School of Mechanics and Civil Engineering, China University of Mining and Technology, Xuzhou 221116, People's Republic of China

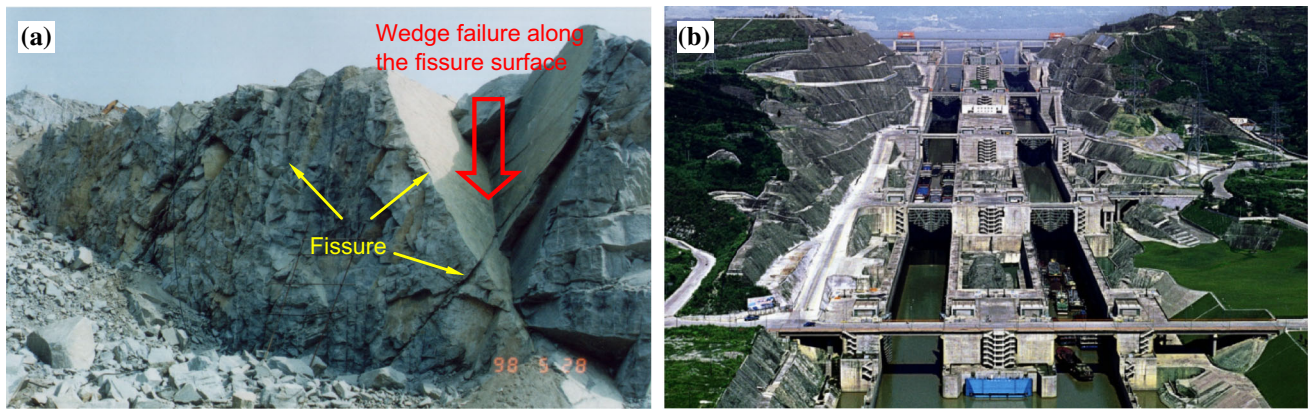


Fig. 1 Three Gorges Project located in Yichang city, Hubei province, China. **a** Granite rock mass high slope (modified after Shi 2006); **b** double-lane five-step ship lock (after Fan et al. 2015)

Wong and Einstein 2009; Lee and Jeon 2011; Yang and Jing 2011; Zhang and Wong 2012). Fujii and Ishijima (2004) performed uniaxial compression tests on sandstone specimens with an inclined slit or an inclined initial fracture from the specimen surface. The experimental results showed the crack from the inclined slit from the specimen surface grew at a small angle to the initial direction and curved slightly toward the free surface in all cases for sandstone specimens. Lu et al. (2008) conducted an experimental study on cylindrical red sandstone (50 mm in diameter and 100 mm in length) containing one preexisting fissures under chemical action, which investigated the influence of water chemistry on the mechanical behavior of pre-cracked sandstone. Wong and Einstein (2009) investigated the cracking behaviors in modeled gypsum and Carrara marble specimens containing a single open fissure under uniaxial compression. Yang and Jing (2011) conducted uniaxial compression experiments for brittle sandstone specimens containing a single fissure. Based on the experimental results of axial stress–strain curves, the influence of fissure length and fissure angle on the strength, deformation and cracking behavior of sandstone specimens has been analyzed in detail. They found that the uniaxial compressive strength, elastic modulus, deformation modulus and peak strain all decrease with the increase in fissure length, but first decrease then increase with increasing fissure angle. Nine different crack types were identified based on the geometry and crack propagation mechanism in their study. However, the above experimental studies are mainly limited under uniaxial compression stress state.

As many people know, the TGP is the largest hydro-power project in the world and has a double-lane five-step ship lock, as shown in Fig. 1b (Fan et al. 2015). The side slopes of the lock are characterized by great height (170 m), steepness (70 m in height of upright slope) and length (over 7000 m in total length). All of the rocks in the TGP are all granite with different amounts of weathering.

To evaluate the stability and safety of the steeply sloping lock channel, many experiments have been performed on the granite specimens from the TGP. Yu and Yin (2004) compared the energy dissipation characteristics of TGP granite under four different loading modes (3-point bending, Brazilian tension, uniaxial compression and triaxial compression) and determined that a 3-point bending specimen dissipated minimum energy, a Brazilian tension specimen dissipated much more energy than a 3-point bending specimen but less than a uniaxial compression specimen, and a triaxial compression specimen dissipated maximum energy. Zhu et al. (2007) conducted conventional triaxial compression tests on the TGP granite, which showed that the crack initiation stress of the granite generally occurred between 25 and 50% of the peak strength. In addition to experimental results on granite from the TGP, Zhao et al. (2013) experimentally studied the deformation, peak and post-peak strength characteristics of granite from Beishan area (a preferable region for high-level radioactive waste disposal in China) under uniaxial and triaxial compression. Using a three-dimensional (3-D) acoustic emission (AE) monitoring system, Chen et al. (2014) experimentally studied the cracking process of Beishan granite under compressive stress condition and its effect on the hydro-mechanical properties. Sun et al. (2015) investigated the physical and mechanical behaviors of granite specimens after high-temperature treatment under uniaxial compression.

However, previous triaxial compression experiments have rarely been conducted for granite materials containing 3-D fissures, and the failure mechanical behavior of fissured granites is not well known due to the difficulty of conducting triaxial experiments on fissured rocks. Further, X-ray computed tomography (CT) is an effective noninvasive nondestructive method to detect the internal fracture in a material. In recent years, CT scanning has been applied to explore the internal damage behavior of rock (Jia et al.

2013; Zhao et al. 2014; Lu et al. 2015; Wang et al. 2015; Yang et al. 2015, 2017; Zhao et al. 2017). However, X-ray CT observations have rarely been applied to fissured granites under triaxial compression. Therefore, in this paper, we report the results of a series of conventional triaxial compression tests on granite containing a single fissure under different confining pressures ranging from 0 to 20 MPa. Based on the experimental results, we first investigate the influence of the angle of a single fissure on the deformation parameters of granite material to evaluate the crack damage threshold and peak strength behavior of granite containing a single fissure under conventional triaxial compression. Then, we analyze the effects of the angle of the single fissure and the confining pressure on the crack types of granite. Finally, using an X-ray microCT scanning system, the internal damage characteristics of the deformed granite specimens containing a single fissure are analyzed in detail.

Experimental methodology

Granite material

To investigate the mechanical behavior of rock with one preexisting open fissure, the granite material located in Quanzhou city of China was chosen for the experimental study in this research. The granite has a crystalline and blocky structure (Fig. 2) and is macroscopically very homogeneous with an average unit weight of approximately 2730 kg/m^3 . The mineral components of the tested granite material are muscovite (46.04%), quartz (10.32%), labradorite (37.69%) and hornblende (5.95%) according to XRD analysis.

In this research, thirty-one granite specimens were prepared to perform uniaxial and conventional triaxial compression tests with the confining pressure equal to 0, 5, 10, 20 and 30 MPa. The specimens were drilled from one big rectangular block. During the process of drilling, we

machined the granite specimens along the same direction in order to avoid the influence of anisotropy on the experimental results for the granite. At the same time, machined granite specimens were observed and carefully selected to produce specimens suitable for testing. To obtain the exact results as well as the best comparison, all the experiments were performed in natural and dry conditions.

According to the method suggested by the International Society for Rock Mechanics (ISRM) (Fairhurst and Hudson 1999), the length-to-diameter ratio of tested specimens should be in the range of 2.0–3.0 to minimize the influence of the end friction effects on the testing results. Therefore, all tested granite specimens are cylinders of 38 mm in diameter and 80 mm in length. As a result, all tested specimen have a length-to-diameter ratio of 2.1 to ensure a uniform stress state within the specimens. The strength behaviors of specimens under conventional triaxial compression tests are also determined according to the method suggested by the ISRM.

The geometry of a granite specimen containing a preexisting single fissure is illustrated in Fig. 3. The fissure length is $2a$, and the fissure angle (the angle between the fissure and the direction of the confining pressure) is α . To simplify the present analysis, the fissure length $2a$ is fixed at 14 mm. A high pressure water-jet cutting technique was used to cut 3-D open single fissure in the intact specimens. The machined fissure width is approximately 1.8–2.0 mm. To investigate the effect of preexisting crack geometry on the strength and deformation behavior of granite under different confining pressures, five fissure angles ($\alpha = 0^\circ, 30^\circ, 45^\circ, 60^\circ$ and 90°) were chosen for this study. Detailed descriptions for granite specimens with different fissure geometries are listed in Table 1.

Testing equipment and procedure

Uniaxial and conventional triaxial compression experiments for intact and fissured granite specimens were all performed on rock servo-controlled triaxial equipment. The equipment

Fig. 2 Microscopic structure of granite used in this research. **a** Optical microscopy, and **b** SEM photograph

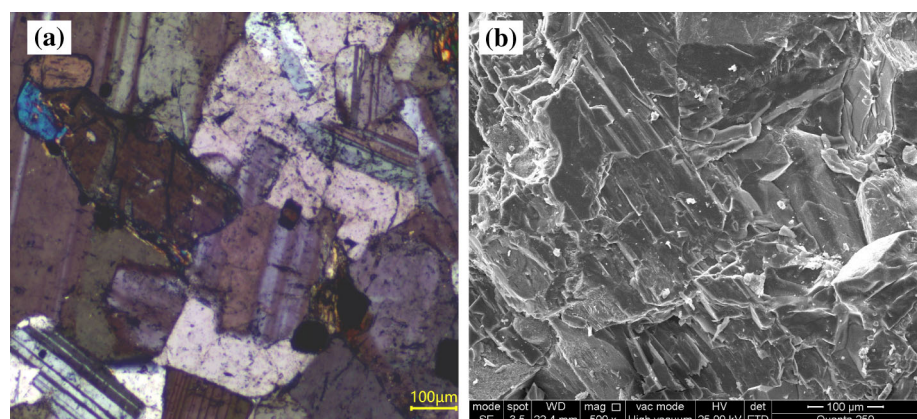


Fig. 3 Granite specimen containing preexisting 3-D single fissure

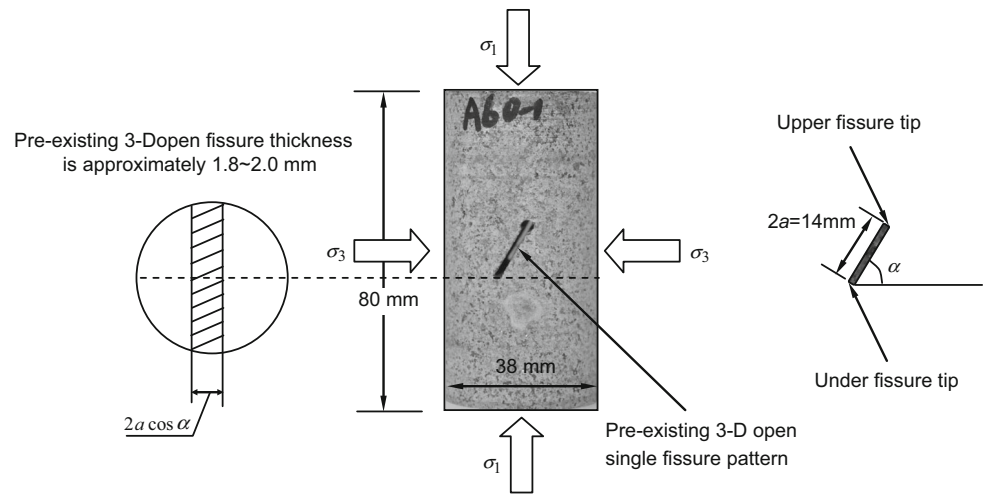


Table 1 Preexisting single fissure geometries of granite specimens

Fissure geometry	Specimen number	D/mm	L/mm	$2a/mm$	σ_3/MPa
Intact specimen	I2 [#]	38.2	78.4	N/A	0
	I3 [#]	37.9	76.5	N/A	5
	I7 [#]	38.2	76.4	N/A	10
	I11 [#]	38.1	76.4	N/A	20
	I13 [#]	38.1	73.8	N/A	30
$\alpha = 0^\circ$	A0-1 [#]	38.3	80.0	14	0
	A0-6 [#]	38.5	80.1	14	0
	A0-2 [#]	38.4	80.0	14	5
	A0-3 [#]	37.9	78.7	14	10
	A0-4 [#]	38.3	80.5	14	20
	$\alpha = 30^\circ$	A30-1 [#]	37.7	80.5	14
A30-16 [#]		38.0	79.8	14	0
A30-2 [#]		38.3	80.0	14	5
A30-3 [#]		38.2	81.0	14	10
A30-5 [#]		38.4	80.9	14	10
A30-7 [#]		38.3	78.9	14	20
$\alpha = 45^\circ$	A45-1 [#]	38.2	80.1	14	0
	A45-3 [#]	38.0	80.8	14	5
	A45-6 [#]	38.0	80.9	14	10
	A45-5 [#]	38.0	81.3	14	20
$\alpha = 60^\circ$	A60-1 [#]	38.0	80.7	14	0
	A60-2 [#]	38.0	79.8	14	0
	A60-6 [#]	37.9	81.0	14	5
	A60-4 [#]	38.1	80.4	14	10
	A60-5 [#]	38.0	80.4	14	20
$\alpha = 90^\circ$	A90-1 [#]	38.0	81.0	14	0
	A90-6 [#]	38.0	80.0	14	0
	A90-3 [#]	38.4	79.4	14	5
	A90-2 [#]	38.0	80.3	14	10
	A90-4 [#]	38.0	81.6	14	20
A90-5 [#]	38.0	79.1	14	20	

D diameter, L length

included a loading system, constant-stability pressure equipment, a hydraulic pressure transfer system, a pressure chamber, a hydraulic pressure system, and an automatic data collection system. The most important part of this equipment is the self-equilibrium triaxial pressure chamber system, which consists of three high precision pumps controlling axial pressure, confining pressure, and pore pressure. The maximum capacity of confining pressure and pore pressure is 60 MPa. However, the maximum capacity of axial pressure can reach approximately 800 kN. Due to the auto-compensation system, the axial pressure generated by axial pressure pump is transmitted entirely as deviatoric stress. The testing equipment can be used to perform all controlled tests, and the data acquisition and analysis by computer and automatized operations ensure that the tests are conducted safely and precisely and performed in a timely manner. The data are collected automatically by the digitized computer configuration. This equipment can be used to perform hydrostatic pressure tests, conventional triaxial compression tests under drained or undrained conditions, triaxial seepage tests, triaxial creep tests, and chemical corrosion tests, etc.

The triaxial compression experiment procedure is described as follows: The confining pressure was first applied to the specimen at a constant rate of 0.5 MPa/s, which ensured that the specimen was under uniform hydrostatic stresses; then, the axial deviatoric stress was applied to the surface of the rock specimen at a 0.04 mm/min displacement control rate until the failure occurred. During the entire uniaxial and triaxial compression experiment, loads and deformations of the tested granite specimens were recorded simultaneously. Moreover, two rigid steel cylinders (38 mm in diameter and 20 mm in length) were placed between the loading frame and the rock specimen, which distinctly decreased the influence of the end friction effects on the testing results of granite specimens with a length-to-diameter ratio of ~ 2.0 . During a test, the axial displacement was measured with two linear variable differential transformers (LVDTs), as shown in Fig. 4, which were fixed between the bottom and top surfaces of the specimen inside the triaxial cell. The circumferential strain transformer was wrapped around the central region of the specimen.

Triaxial experimental results of granite containing a single fissure

To analyze the discreteness of the tested granite specimens, we repeated tests with several specimens under the same experimental conditions. Figure 5 presents a typical effect of specimen variability on the triaxial stress–strain curves of granite containing a single fissure ($\alpha = 90^\circ$).

In Fig. 5, σ_1 and σ_3 represent the major principal stress and the confining pressure, respectively. ε_1 and ε_3 represent

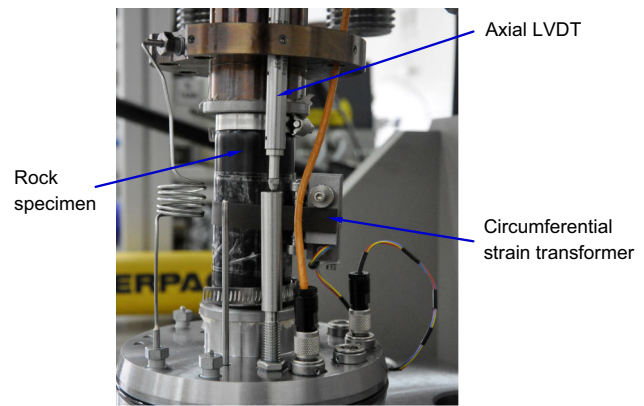


Fig. 4 Strain measurement of granite in the present study

the axial strain and the circumferential strain, respectively. In this research, a positive value for the strain means compressive deformation and a negative value means dilatation deformation. From Fig. 5, the standard deviations of the elastic modulus, axial peak strain and triaxial compressive strength under axial compression for $\alpha = 90^\circ$ are 1.98 GPa, 0.3815×10^{-3} and 2.96 MPa, while they are 1.985 GPa, 0.0745×10^{-3} and 2.49 MPa under a confining pressure of 20 MPa for $\alpha = 90^\circ$. It can be seen that specimen variability has a minimal influence on the deformation behavior of fissured granite specimens. Therefore, based on a series of conventional triaxial test results of fissured granite specimens, we can analyze the influence of the confining pressure and the fissure angle on the deformation parameters of the tested granite material.

Deformation behavior of granite containing a single fissure

Axial deviatoric stress–strain curves of granite containing a single fissure with different fissure geometries under conventional triaxial compression are shown in Fig. 6, in which the numbers give the confining stress in MPa. From Fig. 6, we can conclude that the yielding stress (the stress value that begins to depart from the linear elastic phase in the axial stress–strain curve) and TCS (triaxial compressive strength) of intact and fissured specimen increase gradually with the confining pressure.

In accordance with Fig. 6, the axial deviatoric stress–strain curves of intact and fissured granite at the lower confining pressures initially show nonlinear deformation, and this usually results from the closure of open microcracks (Yang et al. 2012b). It is known that a minor load may result in a large deformation due to the closure of open microcracks in the rock specimen, and thus, the macroscopic stress–strain curve is nonlinear. Moreover, this stage of microcrack closure depends on the confining pressure. With the increase in confining pressure, the stage of

Fig. 5 Typical effect of heterogeneity on axial deviatoric stress–strain curves of granite containing preexisting single fissure for $\alpha = 90^\circ$. **a** $\sigma_3 = 0$ MPa. **b** $\sigma_3 = 20$ MPa

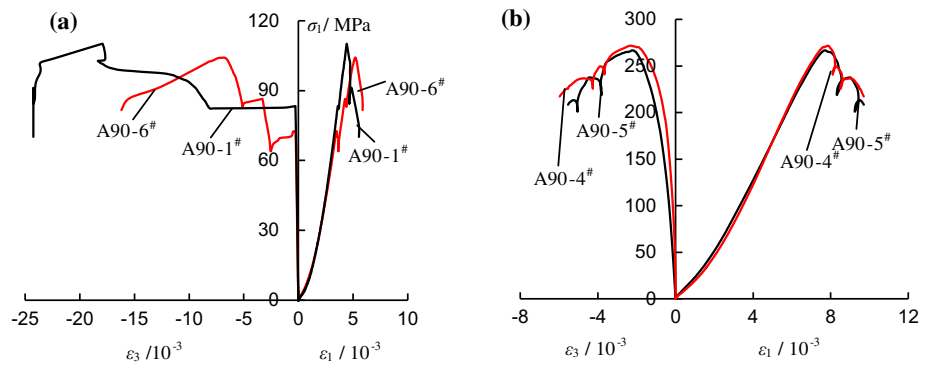
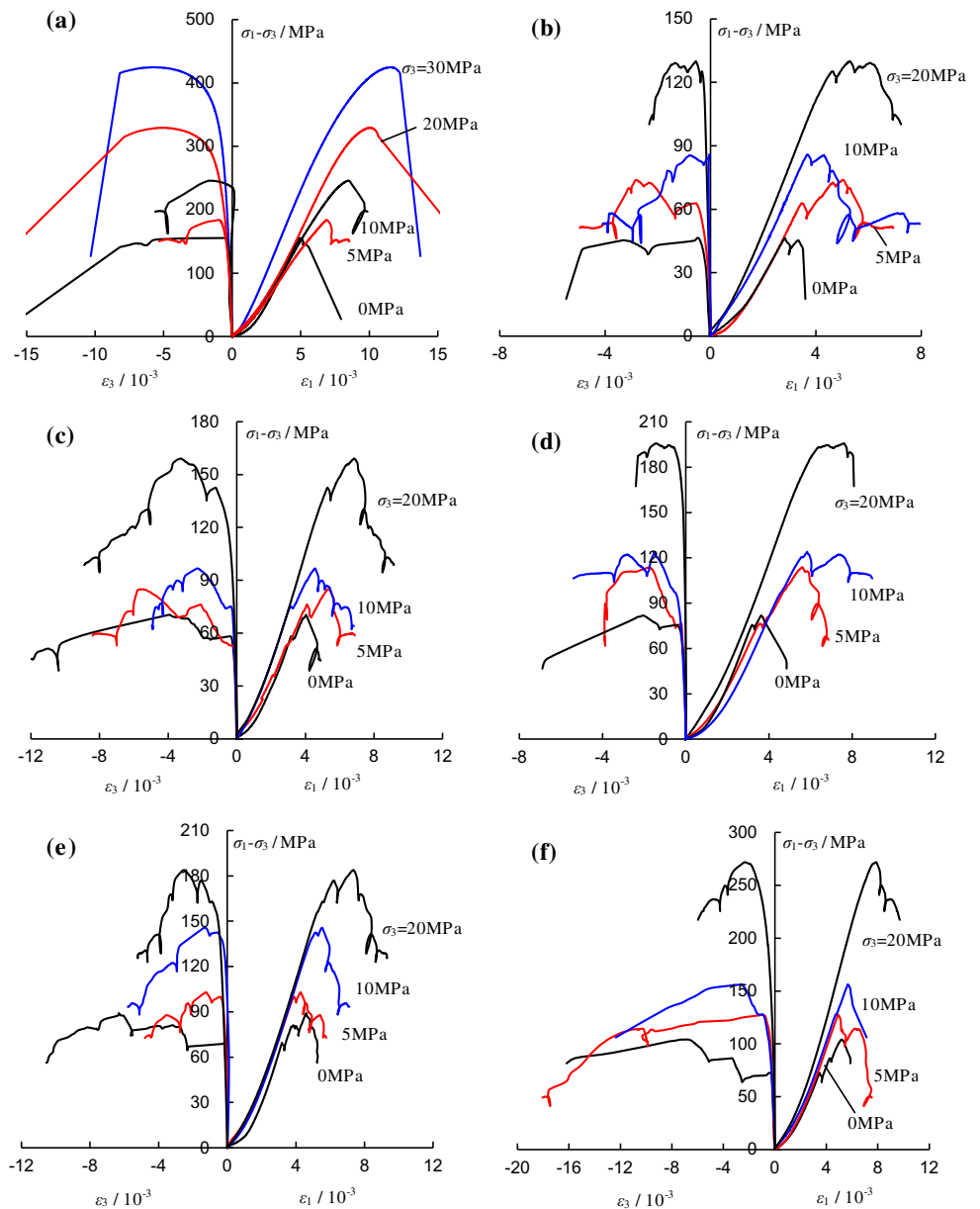


Fig. 6 Axial deviatoric stress–strain curves of granite containing a single fissure with various fissure angles. **a** Intact specimen. **b** $\alpha = 0^\circ$. **c** $\alpha = 30^\circ$. **d** $\alpha = 45^\circ$. **e** $\alpha = 60^\circ$. **f** $\alpha = 90^\circ$



initially nonlinear deformation becomes less and less distinct. This is likely to be a result of the confining pressure acting to close the preexisting microcracks prior to the start

of deformation. After the stage of microcrack closure, the stage of elastic deformation dominates the linear portions of the stress–strain curves. With continuous increase in

axial deformation, the stress–strain curves begin to depart from the linear behavior, which marks the yielding of the specimens. However, when the peak strength is reached, there is an obviously brittle drop. It should be noted that the granite specimens have no clear residual strength. In the stress–strain curves, there are many stress drops, which result from the initiation and propagation of cracks inside the granite specimen; however, the location and numbers of stress drop are closely related to the fissure angle.

Based on the experimental results shown in Fig. 6, Table 2 lists the deformation parameters of granite specimens containing a single fissure under conventional triaxial compression. In Table 2, E_S is the elastic modulus, which is confirmed by the slope of the approximately linear part of the stress–axial strain curve (Yang et al. 2008). ε_{1c} is the peak axial strain value at rupture in terms of the stress–axial strain curve.

According to E_S and ε_{1c} values listed in Table 2, Fig. 7 illustrates the effect of confining pressure on the elastic modulus and the peak axial strain of granite containing a single fissure with various fissure angles. From Fig. 7a, we conclude that the elastic modulus of an intact granite specimen decreases from 43 to 32.74 GPa as σ_3 increases from 0 to 5 MPa. This can be explained as follows. Compared with uniaxial compression, the axial deformation of the granite specimen is larger than the circumferential deformation under a 5 MPa hydrostatic pressure, which results in the decrease in E_S . However, the elastic modulus increases linearly from 32.74 to 50.11 GPa as σ_3 increases from 5 to 30 MPa because the confining pressure increases the stiffness of the granite due to the increasing closure of many pores and fissures in the specimen.

In addition, from Fig. 7b and Table 2, it can be concluded that the elastic moduli of fissured specimens are all smaller than those of intact specimens, which can be explained as follows. Due to the heterogeneity of the rock material, the existence of a single fissure in the specimen results in the increase in the slipping interface; therefore, the slippage of fissured specimen also increases in the process of axial compression, which reduces the elastic modulus of fissured granite. Moreover, because the crack evolution modes in the fissured granite specimen vary greatly with the fissure angle, the elastic modulus of fissured granite has no quantitative relation with the fissure angle. However, except for uniaxial compression, the elastic modulus of fissured granite increases nonlinearly with increasing confining pressure, and the increasing amplitude is slower than for an intact specimen.

The intact granite specimens failed at an axial strain of approximately 0.50–1.16% under different confining pressure, which is greater than that of the fissured granite specimens. Moreover, we find that ε_{1c} of an intact specimen increases linearly with increasing σ_3 , as shown in

Fig. 7c. However, for fissured granite, the failure axial strain usually ranges from 0.20 to 7.86% and increases nonlinearly with increasing σ_3 for the same angle of single fissure, as shown in Fig. 7d; the value of failure axial strain is significantly dependent on the cracking mode in the fissured specimens under different confining pressures.

Crack damage threshold and peak strength of granite containing a single fissure

A typical evolution of the volumetric strain of a fissured granite specimen under conventional triaxial compression is shown in Fig. 8. ε_v refers to the volumetric strain, which is calculated from the sum of ε_1 and twice ε_3 (i.e., $\varepsilon_v = \varepsilon_1 + 2\varepsilon_3$). The crack damage threshold (σ_{cd}) of the specimen (Wong et al. 1997; Fairhurst and Hudson 1999; Heap et al. 2009) is defined as the corresponding axial deviatoric stress at which the volumetric deformation of the specimen switches from compaction-dominated to dilatancy-dominated. The peak strength (σ_p) is obtained by the maximum stress value in the deviatoric stress–strain curves. The crack damage thresholds and the peak strengths of granite specimens with respect to various fissure angles are listed in Table 2.

To investigate the effect of confining pressure on the strength and crack damage behavior of granite specimens with various fissure angles, a common Mohr–Coulomb criterion is adopted in the present study. The linear Mohr–Coulomb criterion can be expressed with the following equation:

$$\sigma_S = M + N\sigma_3 = \frac{2C \cos \varphi + \sigma_3(1 + \sin \varphi)}{1 - \sin \varphi} \tag{1}$$

where σ_S is the maximum axial supporting capacity of the rock; M and N is the material parameters, which are related to the cohesion C and the internal friction angle φ of the rock material.

In accordance with Mohr–Coulomb criterion Eq. (1), the influences of the confining pressure on the crack damage threshold and the peak strength for granite specimens are presented in Figs. 9 and 10, respectively. It is very clear that there are good linear regression coefficients of $R = 0.932$ – 0.998 for the crack damage threshold, and $R = 0.972$ – 0.998 for the peak strength. Tables 3 and 4 list the crack damage and the peak strength parameters, respectively, in accordance with the linear Mohr–Coulomb criterion.

Based on Figs. 9, 10 and Tables 3, 4, it is clear that M and N are 152.24 MPa and 7.75, respectively, for the crack damage threshold, while M and N are 149.24 MPa and 10.13, respectively, for the peak strength; these observations result in the following conclusion. The C_{cd} of intact granite is 27.34 MPa, which is higher than C_p of

Table 2 Mechanical parameters of granite specimens containing a single fissure under conventional triaxial compression

Fissure geometry	Specimen number	σ_3 /MPa	E_S /GPa	$\varepsilon_{1c}/10^{-3}$	σ_{cd} /MPa	σ_{sd} /MPa	σ_P /MPa	σ_S /MPa
Intact specimen	I2 [#]	0	43.00	4.982	152.96	152.96	155.60	155.60
	I3 [#]	5	32.74	6.876	181.08	186.08	183.95	188.95
	I7 [#]	10	37.54	8.512	232.98	242.98	245.94	255.94
	I11 [#]	20	44.33	10.086	270.64	290.64	329.49	349.49
	I13 [#]	30	50.11	11.583	362.00	392.00	424.89	454.89
$\alpha = 0^\circ$	A0-1 [#]	0	21.51	2.821	43.08	43.08	46.39	46.39
	A0-6 [#]	0	26.03	2.011	39.22	39.22	43.52	43.52
	A0-2 [#]	5	23.44	5.032	57.95	62.95	73.82	78.82
	A0-3 [#]	10	29.69	3.678	85.42	95.42	85.87	95.87
	A0-4 [#]	20	31.03	5.292	129.54	149.54	129.99	149.99
$\alpha = 30^\circ$	A30-1 [#]	0	31.33	2.827	–	–	70.22	70.22
	A30-16 [#]	0	23.14	4.036	55.74	55.74	70.44	70.44
	A30-2 [#]	5	20.24	5.385	52.85	57.85	84.99	89.99
	A30-3 [#]	10	28.75	4.557	72.83	82.83	96.77	106.77
	A30-5 [#]	10	25.01	4.249	91.18	101.18	93.38	103.38
$\alpha = 45^\circ$	A30-7 [#]	20	31.84	6.825	120.95	140.95	159.09	179.09
	A45-1 [#]	0	37.54	4.112	83.16	83.16	100.44	100.44
	A45-3 [#]	5	28.77	5.611	76.33	81.33	113.69	118.69
	A45-6 [#]	10	30.05	5.845	94.21	104.21	124.02	134.02
	A45-5 [#]	20	36.69	7.599	193.02	213.02	195.81	215.81
$\alpha = 60^\circ$	A60-1 [#]	0	33.26	4.610	68.05	68.05	89.15	89.15
	A60-2 [#]	0	30.93	3.848	74.53	74.53	86.10	86.10
	A60-6 [#]	5	29.47	4.270	95.8	100.80	102.95	107.95
	A60-4 [#]	10	34.45	5.526	133.14	143.14	145.67	155.67
	A60-5 [#]	20	35.86	7.349	153.41	173.41	183.78	203.78
$\alpha = 90^\circ$	A90-1 [#]	0	33.10	4.422	83.36	83.36	110.12	110.12
	A90-6 [#]	0	29.14	5.185	72.57	72.57	104.21	104.21
	A90-3 [#]	5	31.84	4.916	111.9	116.90	127.30	132.30
	A90-2 [#]	10	33.87	5.681	103.38	113.38	156.22	166.22
	A90-4 [#]	20	44.81	7.862	226.1	246.10	271.79	291.79
	A90-5 [#]	20	40.84	7.713	219.17	239.17	266.82	286.82

intact granite (23.45 MPa), whereas the φ_{cd} of intact granite is 50.48° , which is lower than φ_P of intact granite (55.12°). However, for fissured granite, M ranges from 39.84 to 74.88 MPa for crack damage threshold, while from 46.66 to 97.16 MPa for the peak strength. Meanwhile, N lies between 4.55 and 8.16 for the crack damage threshold, and between 5.16 and 9.25 for the peak strength. The values of cohesion (C) and internal friction angle (φ) calculated according to the crack damage threshold and the peak strength of granite specimens with a single fissure at five angles are presented in Fig. 11.

Table 3 shows that the values of C_{cd} range from 8.52 to 16.26 MPa, while the values of φ_{cd} are between 39.76° and 51.41° . The above analysis indicates that the values of C_{cd} and φ_{cd} are significantly dependent on the angle of the single fissure in the specimen. Generally, the value of C_{cd} of a fissured granite specimen is considerably lower than

that of an intact specimen, and the value of φ_{cd} is also lower than that of an intact specimen except when $\alpha = 90^\circ$. From Fig. 11, it is clear that with the increase in the fissure angle, the value of C_{cd} of fissured granite specimen first increases nonlinearly from 8.52 to 16.26 MPa as α increases from 0 to 60° , and then decreases to 12.33 MPa as α increases from 60° to 90° . But, the value of φ_{cd} of fissured granite specimens has a nonlinear variance with the increase in fissure angle, and at $\alpha = 90^\circ$, the value of φ_{cd} is approximately 51.41° , which is approximate to that of an intact specimen (50.48°).

In Table 4, the values of C_P range from 10.25 to 18.96 MPa, while the values of φ_P are between 42.48° and 53.60° . The above analysis shows that the values of C_P and φ_P are significantly dependent on the angle of the single fissure in the specimen. Generally, the values of C_P and φ_P of fissured granite specimens are all considerably lower

Fig. 7 Effect of confining pressure on elastic modulus and peak axial strain of granite containing a single fissure with various fissure angles. **a** Elastic modulus of intact specimen. **b** Elastic modulus of fissured specimen. **c** Peak axial strain of intact specimen. **d** Peak axial strain of fissured specimen

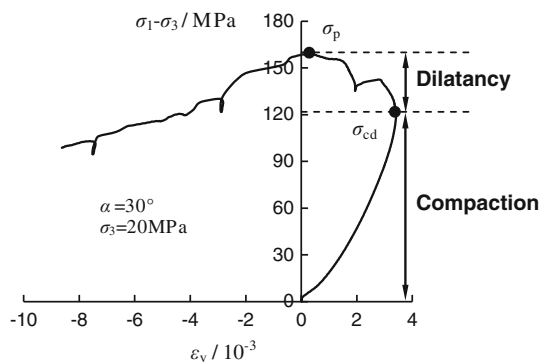
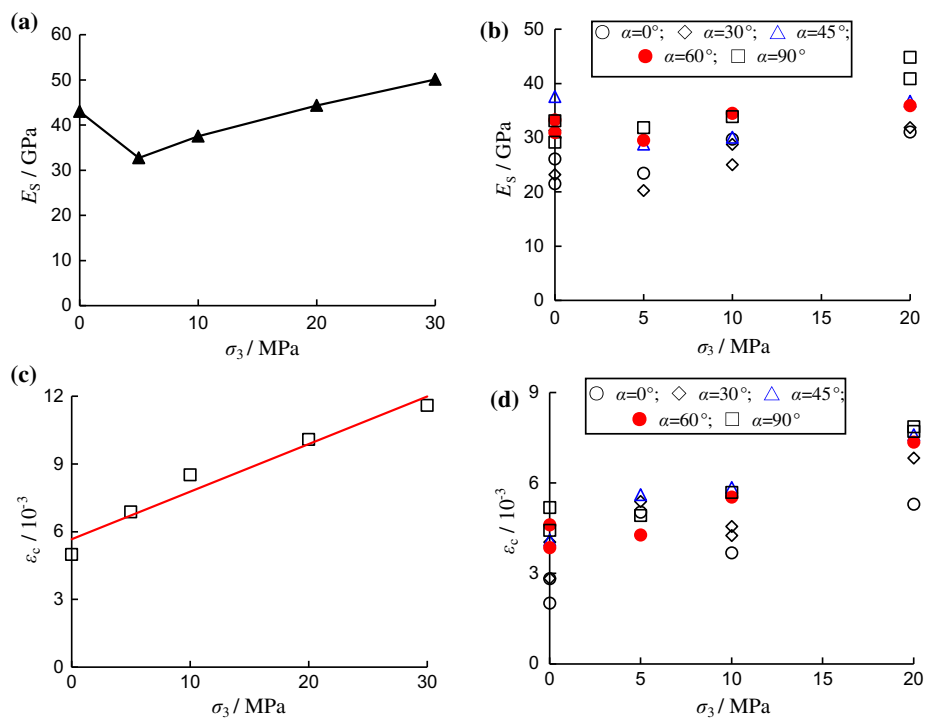
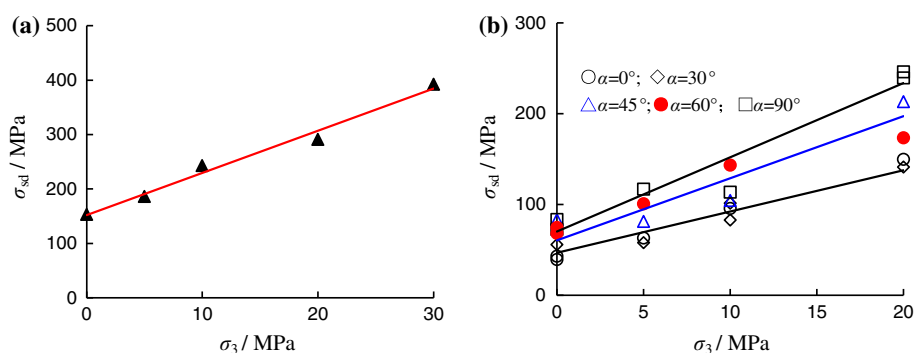


Fig. 8 Confirmation of crack damage threshold and peak strength of fissured granite specimen

than those of intact specimen, even for $\alpha = 90^\circ$. From Fig. 11, it is clear that with the increase in the fissure angle, the value of C_P of fissured granite specimens first increases nonlinearly from 10.25 to 18.96 MPa as α increases from 0

Fig. 9 Influence of the confining pressure on the crack damage threshold of fissured granite specimens. **a** Intact specimen. **b** Fissured specimen



to 45° , and then decreases to 15.97 MPa as α increases from 45° to 90° . However, the value of ϕ_P of fissured granite specimen ranges from 42.48° to 45.52° as α varies between 0 and 60° , but at $\alpha = 90^\circ$, the value of ϕ_P is 53.60° , which is close to that of an intact specimen (55.12°). Furthermore, the cohesion of fissured granite obtained by the crack damage threshold is lower than that obtained by the peak strength, but the internal friction angle of fissured granite obtained by the crack damage threshold is approximately equal to that obtained by the peak strength.

Cracking behavior of granite containing a single fissure

Figure 12 shows the failure modes of intact granite specimens without any preexisting fissures from our conventional triaxial compression experiments. The confining

Fig. 10 Influence of the confining pressure on the peak strength of fissured granite specimens. **a** Intact specimen. **b** Fissured specimen

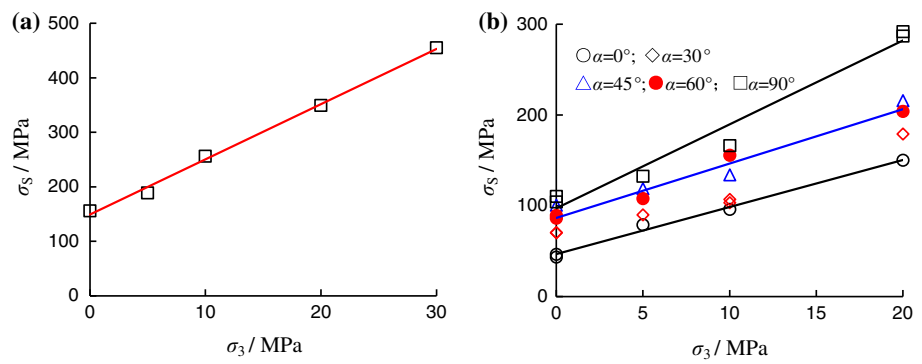


Table 3 Crack damage parameters in accordance with the linear Mohr–Coulomb criterion

Fissure geometry	M/MPa	N	C_{cd}/MPa	$\varphi_{cd}/^\circ$	R
Intact specimen	152.24	7.75	27.34	50.48	0.992
$\alpha = 0^\circ$	39.84	5.46	8.52	43.66	0.998
$\alpha = 30^\circ$	46.74	4.55	10.96	39.76	0.959
$\alpha = 45^\circ$	60.67	6.83	11.61	48.12	0.932
$\alpha = 60^\circ$	74.88	5.30	16.26	43.04	0.979
$\alpha = 90^\circ$	70.42	8.16	12.33	51.41	0.968

Table 4 Peak strength parameters in accordance with the linear Mohr–Coulomb criterion

Fissure geometry	M/MPa	N	C_p/MPa	$\varphi_p/^\circ$	R
Intact specimen	149.24	10.13	23.45	55.12	0.998
$\alpha = 0^\circ$	46.66	5.18	10.25	42.56	0.996
$\alpha = 30^\circ$	64.60	5.16	14.22	42.48	0.972
$\alpha = 45^\circ$	91.38	5.81	18.96	44.94	0.974
$\alpha = 60^\circ$	86.69	5.98	17.73	45.52	0.992
$\alpha = 90^\circ$	97.16	9.25	15.97	53.60	0.986

pressure exerted a significant influence on the failure mode. At confining pressures between 0 and 5 MPa, our granite specimens all demonstrated a typical axial splitting fracture

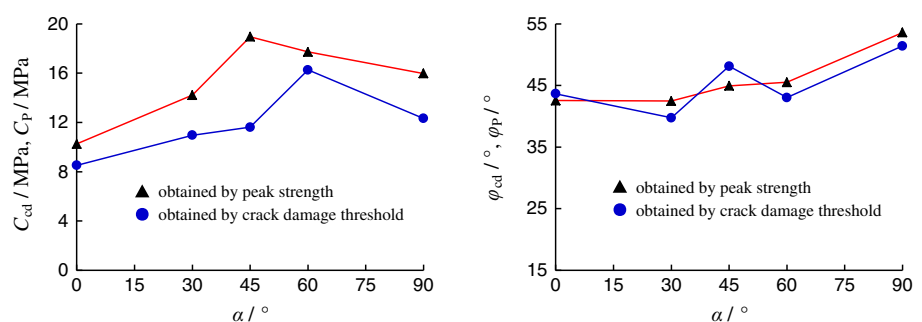
mode, and several axial tensile cracks were observed in the direction of major principal stress. However at confining pressures between 10 and 30 MPa, the granite specimens all demonstrated a typical shear fracture mode. At $\sigma_3 = 10$ MPa, in addition to two main shear fracture planes, several axial and lateral tensile cracks were also observed. At $\sigma_3 = 20$ MPa, two shear cracks were observed; the angle of the left shear fracture plane was approximately 68° , and the angle of right shear fracture plane was approximately 72° . At $\sigma_3 = 30$ MPa, the granite specimen took on a single shear fracture mode. Furthermore, the angle of the shear fracture plane at $\sigma_3 = 30$ MPa was approximately 60° , lower than for $\sigma_3 = 10$ MPa (approximately 68°).

Crack types of granite containing a single fissure

In granite specimens containing a single fissure, crack initiation, propagation and coalescence modes are all observed from the upper and lower tips of the preexisting fissure (Figs. 13, 14), and they are obviously dependent on the confining pressure and the fissure angle. Therefore, in this section, a systematic evaluation is presented on the cracking behavior in granite specimens containing a single fissure under conventional triaxial compression.

Nine different crack types (Fig. 15) were identified based on their geometry and crack propagation mechanism (tensile, shear and far-field crack) by analyzing the ultimate failure modes of granite specimens containing a single

Fig. 11 Influence of fissure angle on crack damage and peak strength parameters of granite specimens



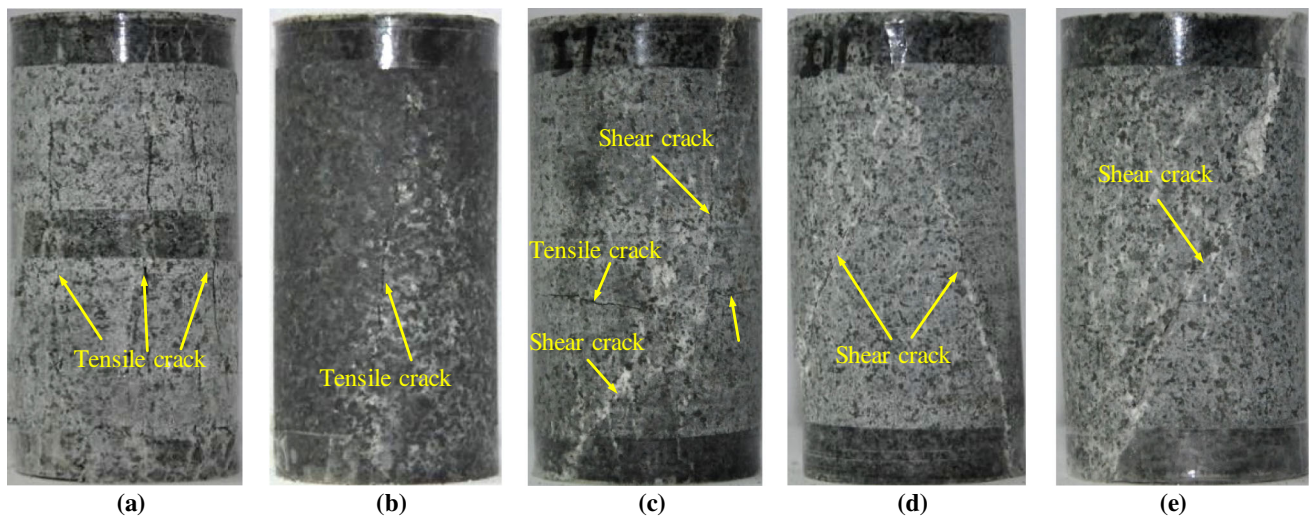


Fig. 12 Ultimate failure mode of intact granite specimen without any preexisting fissures. **a** $\sigma_3 = 0$ MPa. **b** $\sigma_3 = 5$ MPa. **c** $\sigma_3 = 10$ MPa. **d** $\sigma_3 = 20$ MPa. **e** $\sigma_3 = 30$ MPa

fissure (Figs. 13, 14). According to Fig. 15, one can see that four of them (crack types T_w , T_s , T_a and T_{as}) are tensile, three of them (crack types S_m , S_s and S_a) are shear crack, and two of them (crack types F_t and F_s) are far-field. The crack types can be categorized as follows:

1. *Crack type T_w* A tensile wing crack initiates from the upper or lower tips of the single fissure or at a certain distance from the fissure tips. The tensile wing crack usually initiates and propagates along the direction of the major principal stress toward the end surface of the specimen. Moreover due to the influence of crystal grains in granite material, this propagation path of a tensile wing crack T_w is not very smooth.
2. *Crack type T_s* The crack is a secondary tensile crack, which often initiates from upper or lower tip of the single fissure. The crack usually initiates after T_w and propagates along the direction of the major principal stress toward the end surface of the specimen, which is usually the same direction as T_w .
3. *Crack type T_a* The crack propagation is opposite to that of crack type T_w , and therefore, this is called as “anti-tensile crack.” The anti-tensile crack also initiates from the upper or lower tip of the single fissure and develops along the direction of the axial stress.
4. *Crack type T_{as}* The crack propagation follows after T_a , which is called an “anti-tensile secondary crack.” This crack also initiates from the upper or lower tip of the single fissure and develops along the direction of the maximum principal stress.
5. *Crack type S_m* The main shear crack initiates from the upper or lower tip of the single fissure, and the crack initiation path is approximately parallel to the direction of the preexisting fissure. The initiating main shear

crack and preexisting fissure are usually coplanar. However, the main shear crack usually propagates toward the end surface of the specimen along an angle inclined approximately 70° to the minimum principal stress.

6. *Crack type S_s* The secondary shear crack initiates from the upper or lower tip of the single fissure, which usually follows after T_w . The secondary shear crack usually propagates toward the end surface of the specimen along the direction of the maximum principal stress.
7. *Crack type S_a* The anti-shear crack initiates from the upper and lower tip of the single fissure. Although T_a propagates along the direction of the maximum principal stress, S_a propagates toward the corners of the specimen at a smaller angle with the direction of maximum principal stress. Furthermore, S_a propagates in a shear failure mode.
8. *Crack type F_t* The far-field tensile crack does not usually initiate from the tips of the single fissure. Moreover, the far-field tensile crack propagation path is not very smooth, and it may be vertical or horizontal tensile depending on the loading process.
9. *Crack type F_s* The far-field shear crack does not usually initiate from the tips of the single fissure. Moreover, the far-field shear crack coalescence path is not very smooth, and it may have an inclined angle with the direction of the major principal stress.

In accordance with the above nine crack types, one can analyze the ultimate failure mode and cracking process of granite specimens containing a single fissure under triaxial compression (Figs. 13, 14). It is clear that all of the macroscopic failure mode of granite specimens containing

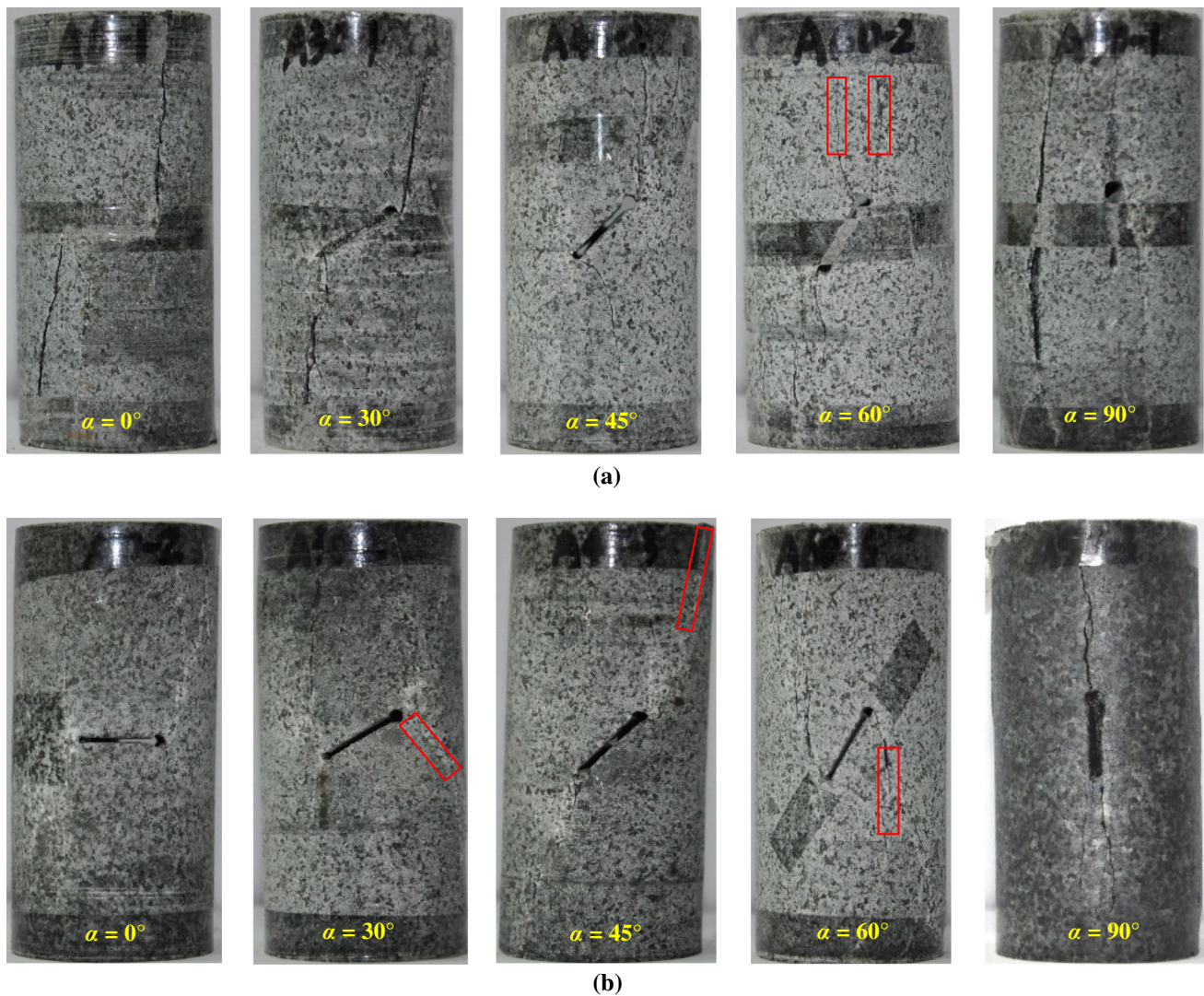


Fig. 13 Ultimate failure mode of granite specimens containing a single fissure at lower confining pressures ($\sigma_3 = 0$ and 5 MPa). **a** Under uniaxial compression ($\sigma_3 = 0$ MPa). **b** At a confining pressure of 5 MPa

a single fissure (Figs. 16, 17) are mixtures of several cracks among the nine various crack types. For example, the failure mode of the specimen with $\alpha = 30^\circ$ and $\sigma_3 = 5$ MPa is a mixture of cracks T_w , T_s , T_a and S_a . It should be noted that typical surfaces of the tensile and shear cracks shown in Figs. 18 and 19 also support initiated crack types depicted in Figs. 16 and 17.

Table 5 summarizes the initiated crack types of granite specimens containing single fissure with different fissure angles in response to the applied axial loads. As indicated in Table 5, under uniaxial compression (see Fig. 16a), T_w is often the first crack and T_s is often a secondary crack that is initiated after T_w . Usually, T_w is initiated from the tips of preexisting fissure. However, sometimes T_w is initiated at a distance away from the tips of the single fissure, but this is observed only in this case of $\alpha = 0^\circ$, which possibly results from the low fissure angle (Yang and Jing 2011). It should

be noted that at the upper fissure tip for $\alpha = 30^\circ$, no T_s cracks are observed from the same position as T_w . For $\alpha = 90^\circ$, no T_s cracks are observed from the upper and lower fissure tips, but the crack T_a is initiated from the upper fissure tip and develops toward the bottom boundary of the specimen along the direction of the maximum principal stress. Moreover, one F_t is observed for $\alpha = 30^\circ$, and several F_t for $\alpha = 60^\circ$ and 90° , which means that it is easier to emanate more far-field tensile cracks with larger fissure angles.

At $\sigma_3 = 5$ MPa, the crack modes in granite specimens containing a single fissure are different from those under uniaxial compression. For $\alpha = 0^\circ$, T_w is initiated from the tips of the single fissure and propagates to the boundaries of the specimen, and several cracks F_t are also observed during the failure. For $\alpha = 30^\circ$, one crack T_w is initiated from the upper fissure tip, but the other crack T_w is initiated

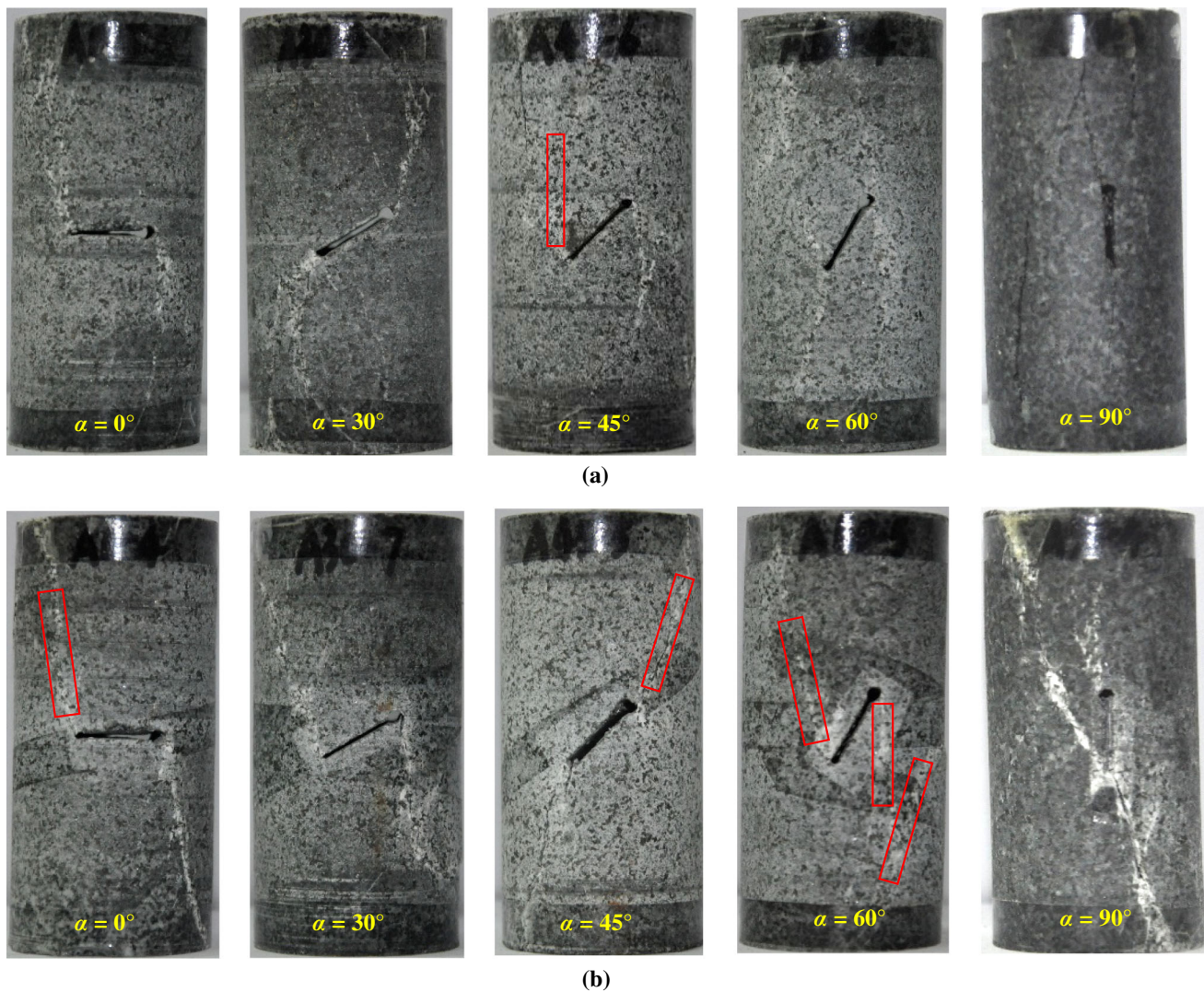


Fig. 14 Ultimate failure mode of granite specimens containing a single fissure at higher confining pressures ($\sigma_3 = 10$ and 20 MPa). **a** At a confining pressure of 10 MPa. **b** At a confining pressure of 20 MPa

at a distance away the lower fissure tip. Although T_s and T_a are observed from the same lower fissure tip, the directions of T_s and T_a are reversed. The anti-shear crack S_a is observed from the upper fissure tip and propagates toward the right boundary of the specimen along the direction perpendicular to the preexisting fissure, and the shear slippage surface is very clear as shown in Fig. 19. For $\alpha = 45^\circ$, one tensile wing crack T_w is initiated from the upper fissure tip and develops as far as the top boundary of the specimen along the direction of the major principal stress, and two shear cracks (S_m and S_s) are observed from the lower and upper fissure tip, respectively. The fracture surfaces of shear cracks are also illustrated in Fig. 19. For $\alpha = 60^\circ$, the anti-tensile crack T_a is observed from the upper and lower fissure tips and propagates to the boundary of the specimen. At the same time, four far-field tensile cracks are observed, and one far-field shear crack emanates

from near the right crack T_a . However, for $\alpha = 90^\circ$, two wing tensile cracks T_w are observed from the upper and lower fissure tips. At the lower fissure tip, two secondary tensile cracks T_s are initiated from the lower fissure tip and develop toward the bottom boundary of the specimen along the direction of the maximum principal stress. Furthermore, three far-field tensile cracks are also observed.

At $\sigma_3 = 10$ MPa, the crack modes in granite specimens containing a single fissure are different from those at $\sigma_3 = 0-5$ MPa. For $\alpha = 0^\circ$, T_w is initiated from the middle position of the single fissure and propagates toward the bottom boundary in the direction of the major principal stress. However, due to the initiation of two cracks from the upper and lower fissure tips, the crack T_w only propagates for a short distance. At the same time, in this specimen, two anti-tensile secondary cracks T_{as} are also observed. Accompanying the ultimate failure, the specimen

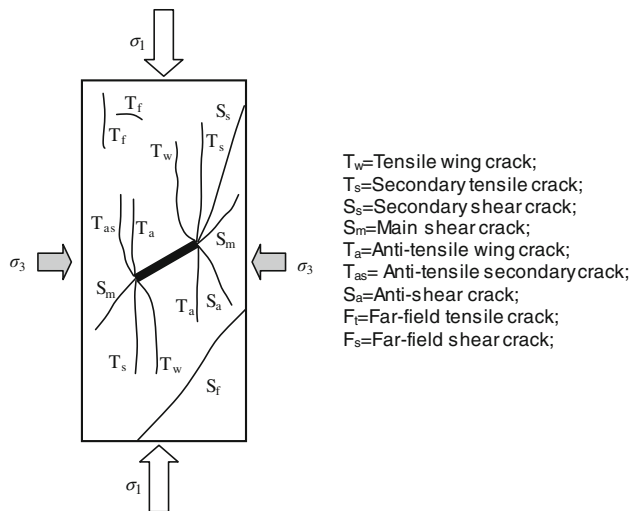


Fig. 15 A sketch of initiated crack types of granite specimens containing a single fissure under conventional triaxial compression (modified after Yang and Jing 2011 and Yang et al. 2012a)

has several far-field tensile cracks. For $\alpha = 30^\circ$, two tensile wing cracks are initiated from the upper and lower fissure tips, and the initiating direction is perpendicular to the preexisting fissure. Then, T_w propagates in the direction of the major principal stress. Afterward, with the increase in axial deformation, two secondary tensile cracks are observed from the same position as T_w and propagate in the direction of the major principal stress. Accompanying the ultimate failure of the specimen, two far-field tensile cracks are also observed. For $\alpha = 45^\circ$, two anti-tensile wing cracks emanate from the upper and lower fissure tips. The left crack T_a does not propagate to the top boundary of the specimen, but the right crack T_a propagates to the bottom boundary of the specimen and the propagation path is not smooth. Accompanying the ultimate failure of the specimen, two far-field tensile cracks are observed in the left top region of the specimen, and one far-field shear crack is observed in the right bottom region of the specimen. For $\alpha = 60^\circ$, the crack mode is very simple; only two anti-tensile wing cracks are observed from the upper and lower fissure tips, and they propagate to the boundaries of the specimen along the direction of the major principal stress. One tensile wing crack is also observed from the lower fissure tip. However, for $\alpha = 90^\circ$, the crack modes are approximately the same as those at $\sigma_3 = 0\text{--}5$ MPa, which indicates that for this fissure angle, the crack mode does not depend on the confining pressure.

At $\sigma_3 = 20$ MPa, the crack modes in granite specimens containing a single fissure are simpler compared to those at $\sigma_3 = 0\text{--}10$ MPa. Furthermore, under higher confining pressure of 20 MPa, the tensile wing and secondary tensile cracks that are easily initiated under lower confining

pressures (0–10 MPa) are restricted; the main-shear and anti-shear cracks dominate the ultimate failure mode of the granite specimen. For $\alpha = 0^\circ$ and 30° , two anti-shear cracks that emanate from the fissure tips dominate the ultimate failure of the specimen. For $\alpha = 45^\circ$, two main shear cracks results in the shear slippage fracture of the specimen. For $\alpha = 60^\circ$, one anti-shear crack is initiated from the lower tip of the single fissure and propagates to the top boundary of the specimen, whereas one anti-tensile crack is initiated from the upper tip of the single fissure and propagates toward the bottom boundary of the specimen. It should be noted that at this fissure angle, one far-field shear crack emanates from the right bottom region of this specimen and one far-field tensile crack is observed in the region under the preexisting fissure. The tensile and shear failure mechanism is also validated from Figs. 18 and 19, respectively. However for $\alpha = 90^\circ$, one main shear crack passes through the entire specimen from the top boundary to the bottom boundary. One tensile wing crack is also observed from the upper tip of fissure and propagates to the top boundary in the direction of the major principal stress. At the same time, one far-field shear crack is observed in the left middle region accompanying the ultimate failure of the specimen.

It should be noted that shear crack S_a and S_m are usually easier to initiate and nucleate for larger confining pressures, e.g., the confining pressure is 20 MPa. However, for $\sigma_3 = 5$ MPa, only the specimen with $\alpha = 45^\circ$ initiates shear cracks S_m and S_s , and the specimen for $\alpha = 30^\circ$ initiates shear cracks S_a . Tensile cracks T_w and T_s are easier to emanate for lower confining pressure (0–10 MPa), but for $\alpha = 90^\circ$, the tensile wing crack T_w is observed in all of the specimens. It is very clear that T_s often accompanies with T_w toward the same direction. T_a is usually easier under the action of confining pressure, except for $\alpha = 90^\circ$. In accordance with Table 5, the anti-tensile secondary crack T_{as} is rare, observed only for $\alpha = 0^\circ$ and $\sigma_3 = 10$ MPa. However, far-field tensile cracks initiate in most of the specimens containing a single fissure, and far-field shear cracks initiate only under the larger confining pressures.

From Figs. 16 and 17, it can also be observed that several wing tensile cracks T_w appear to stop at a certain distance from the upper and lower boundaries of the specimen, which is probably related to the confining stress induced by the friction between the specimen and the steel plates at $\sigma_3 = 0$ MPa or the constriction of applied confining pressure. The tensile fracture and shear fracture of granite specimens under conventional triaxial compression can be further inferred from microscopic observations on the fracture surface of the failed specimen, as shown in Figs. 18 and 19. The microscopic structure images were obtained using KH-8700E optical microscopic machine.

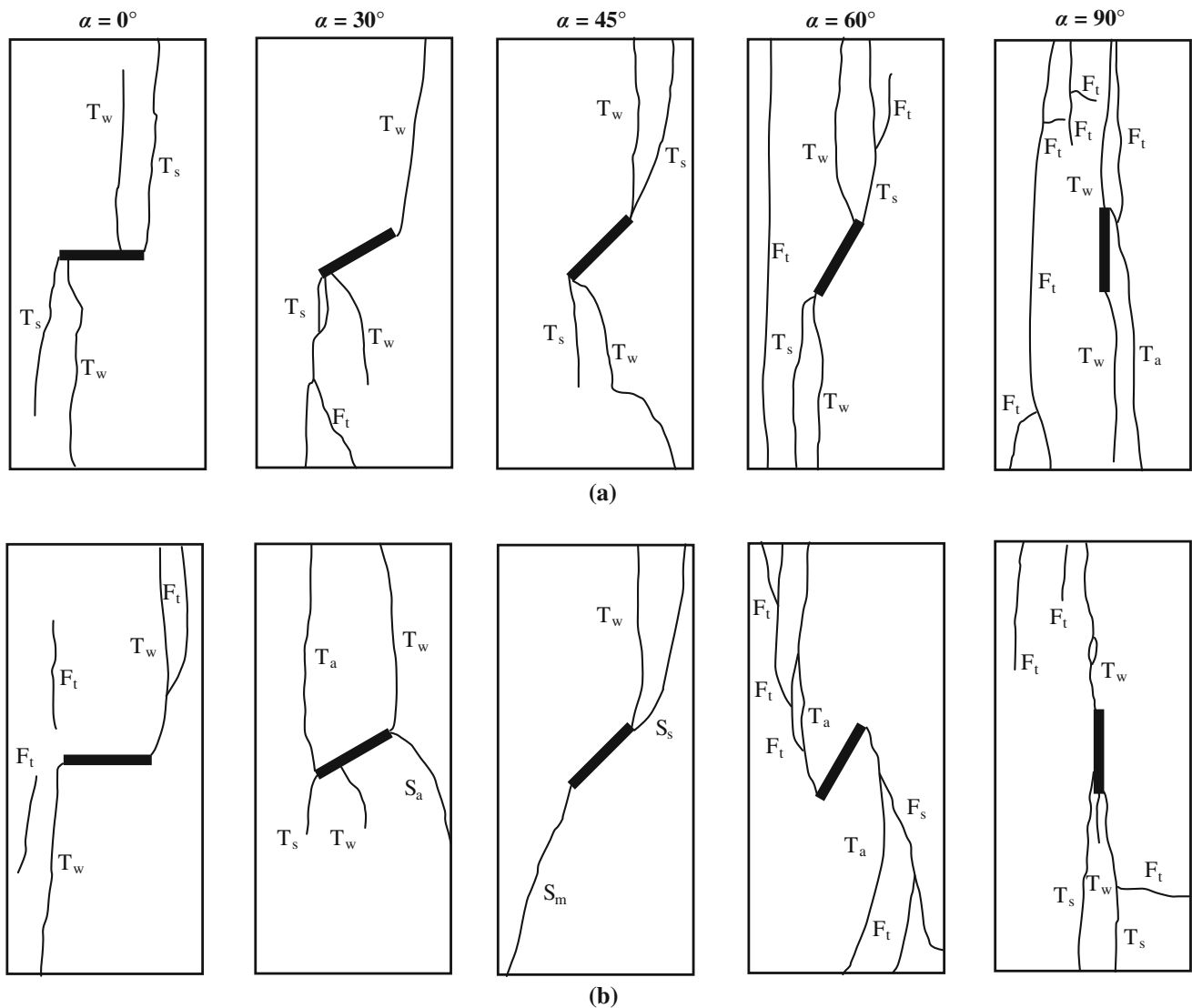


Fig. 16 Crack types of granite specimens containing a single fissure at lower confining pressures ($\sigma_3 = 0$ and 5 MPa). **a** Under uniaxial compression ($\sigma_3 = 0$ MPa). **b** At a confining pressure of 5 MPa

The tensile fracture is very rough, but the grains keep relatively intact (Fig. 18). However, the shear fracture is very smooth, and slippage powders can be seen (Fig. 19).

Internal crack characteristics of granite by X-ray microCT observation

X-ray CT scanning of the granite specimen was carried out using a Nanotom 160 high-resolution microCT at a spatial resolution of 30 μm . The X-ray beam penetrating the specimen was measured by an array of detectors. The X-ray was produced by electrons striking a Mo–W alloy target in an X-ray tube. The electron current was 80 μA , the

accelerating voltage was 140 kV, and the scanning time was 4 s. The degree of X-ray attenuation depends on the density and the atomic number of the materials in the specimens. Material with higher density and higher atomic number generally causes higher attenuation of the X-rays. X-ray projection data from various directions are obtained by the 360° rotation of the X-ray source. We collected 2-D images at intervals of 0.18°, and thus 2000 slice images could be obtained for one specimen. A 2-D image representing the linear distribution of X-ray attenuation was reconstructed using Fourier transformation of the projection data. A 3-D data set of the specimen was obtained by stacking consecutive 2-D images.

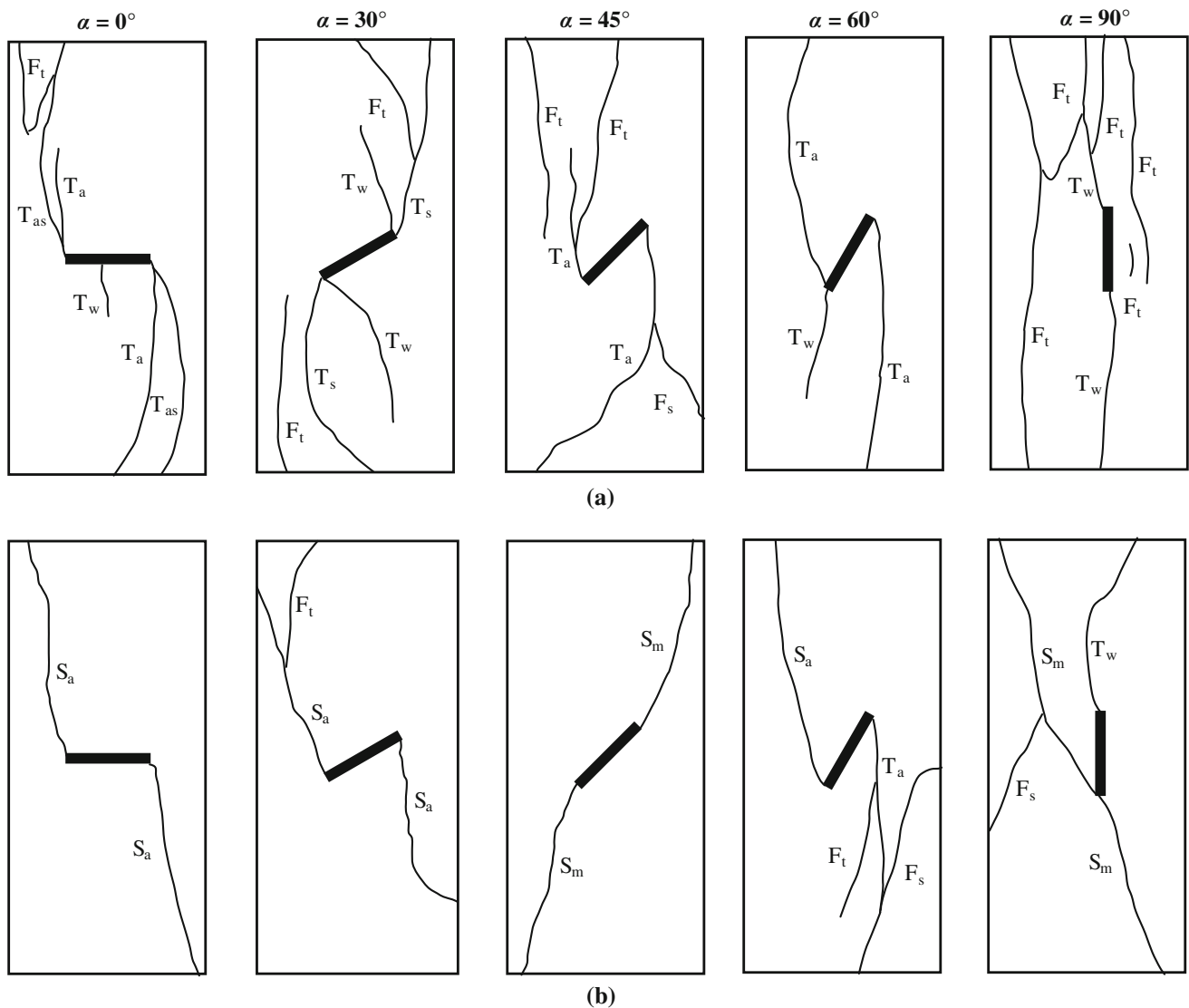


Fig. 17 Crack types of granite specimens containing a single fissure at higher confining pressures ($\sigma_3 = 10$ and 20 MPa). **a** At a confining pressure of 10 MPa. **b** At a confining pressure of 20 MPa

It should be noted that a cylinder only 38 mm diameter and 68 mm length can be regarded as the scanning region, as shown in Fig. 20a, b. Figure 20a, b shows the comparison of the X-ray CT scanning surface images and the actual surface crack photographs of granite specimen containing a single fissure after uniaxial compression failure, where the black regions represent cracks, and other regions indicate no surface failure. In Fig. 20, the X-ray CT scanning surface images approximate the actual surface crack photographs, which demonstrate that X-ray microCT scanning can be used to explore the internal damage in granite materials.

Figure 21 shows 3-D CT images of failed granite specimens. In the 3-D images, the fracture regions are black, and the other regions are transparent. From Fig. 20, the intact granite specimen without any fissures under

uniaxial compression has a typical axial splitting failure mode, which is also identical to the surface fracture shown in Fig. 12a. However, the failure mode of the intact granite specimen after triaxial compression failure is different from that after uniaxial compression failure. At a confining pressure of 10 MPa, the specimen shows a shear failure mode with two shear cracks, along with several localized lateral tensile cracks. However, at a confining pressure of 20 MPa, the specimen takes on a single shear failure mode. By rotating the image of the specimen, the trace of the shear fracture may be perceived as not a plane but a curve.

In contrast, once there exists one preexisting fissure, the granite specimen emanates different crack modes, as shown in Fig. 21e, f. The 3-D fracture of a fissured granite specimen results mainly from the propagation and coalescence of 3-D cracks near the tips of the single fissure.

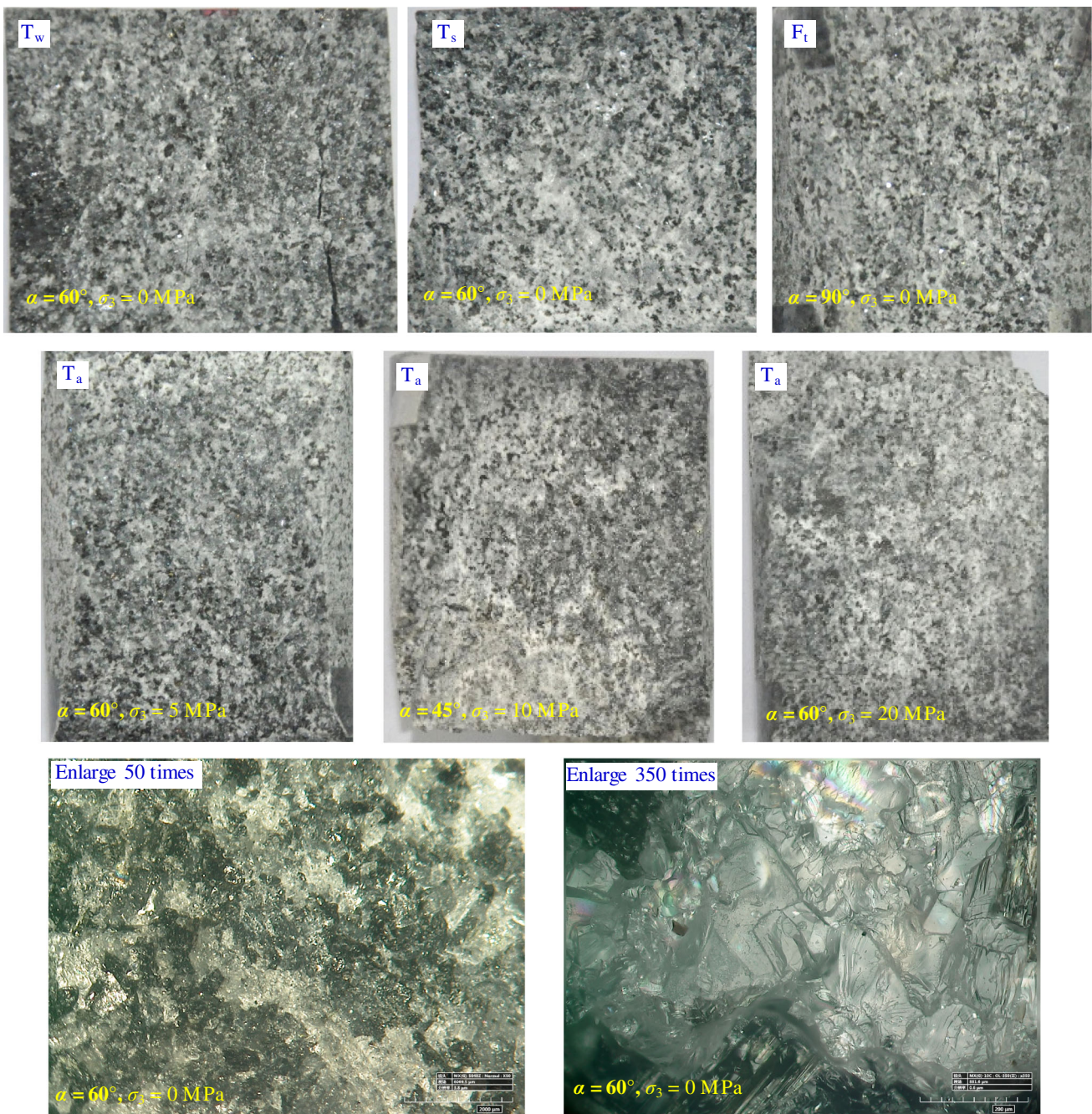


Fig. 18 Observations on tensile crack surface of granite specimens containing a single fissure under conventional triaxial compression

Under uniaxial compression, at a lower fissure angle (e.g., $\alpha = 0^\circ$), it is possible to initiate tensile cracks at a distance away the tips of the preexisting fissure, which was also validated in the previous experimental study for fissured sandstone material (Yang and Jing 2011); however, at larger fissure angles (e.g., $\alpha = 30^\circ$ – 90°), all of the first cracks initiate from the tips of the single fissure. The above analysis indicates that with the increase in the fissure angle, the initiated position of the first cracks transfers from the middle position to the fissure tip. For the same fissure

angle, with the increase in confining pressure, the tensile wing and secondary tensile cracks are restricted; the anti-tensile and anti-shear cracks dominate the ultimate failure mode of the granite specimen. At the same time, due to the effect of the crystal grains in the granite on crack characteristics, the path of crack propagation is not very smooth.

Figure 22 further shows internal vertical CT cross sections of granite specimens containing a single fissure after uniaxial and triaxial compression failure, respectively. From Fig. 22, the width of the fissure is obviously greater than the

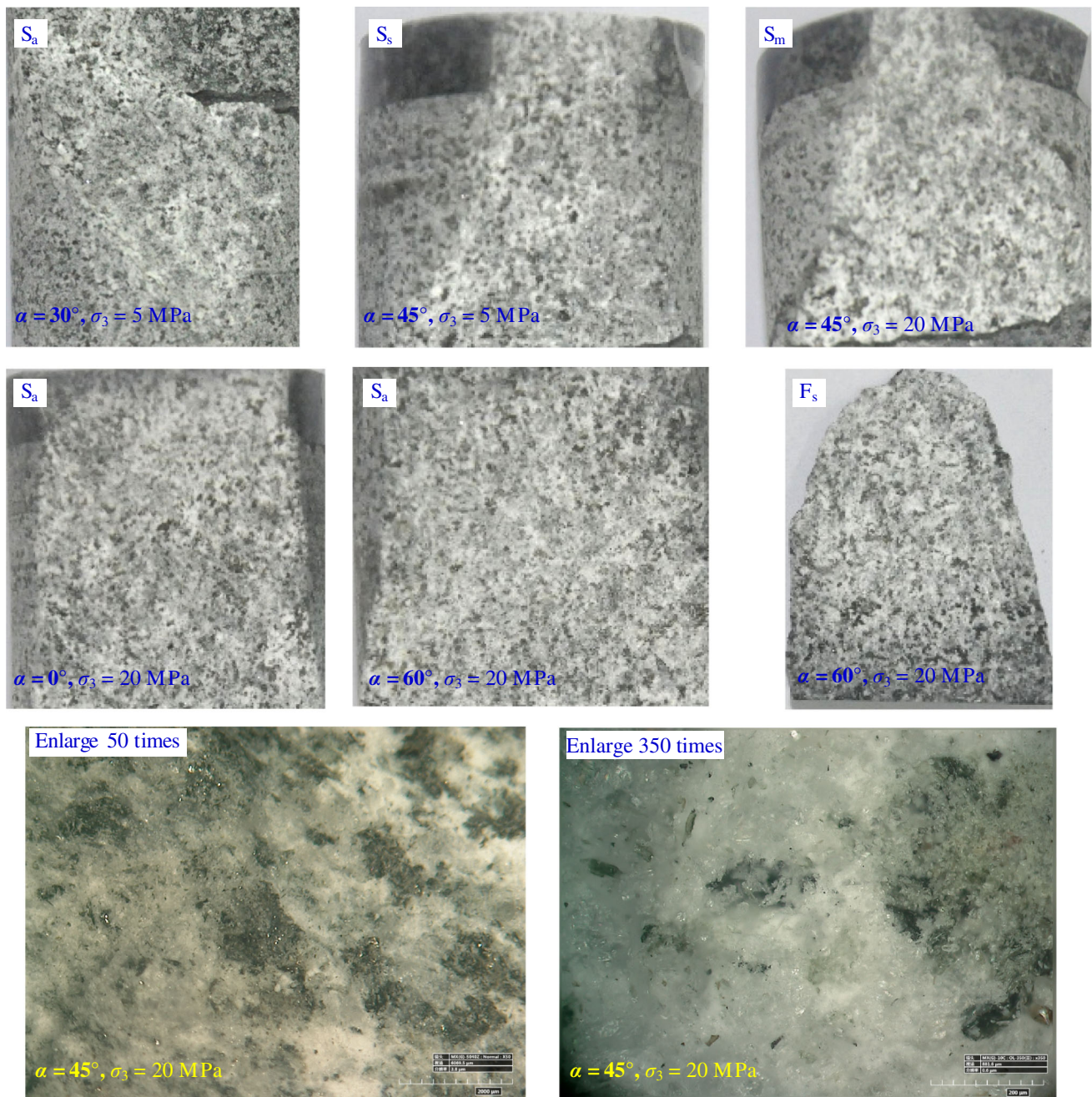


Fig. 19 Observations on shear crack surface of granite specimens containing a single fissure under conventional triaxial compression

other positions at the left tip of the fissure because the water-jet enlarged the hole for the time during which it penetrated the specimen thoroughly (Lee and Jeon 2011). Li et al. (2005) found that the rounded hole has only a little influence on the damage and failure of the specimen. Therefore, the results on the pre-fissured specimens with a slightly larger aperture thickness at its starting point are reliable. Compared Figs. 22 with 21, even though the crack system mode shown in Fig. 21 is three-dimensional CT images, they have still

good similarity. However, we note that at in the fissured granite specimen with $\alpha = 0^\circ$ at $\sigma_3 = 0$ MPa, there is one inclined crack A, which is not observed from Fig. 22, which results from the crack A is one internal crack, as shown in the horizontal cross section. Furthermore, compared Fig. 22f, g, it can be seen that for the same fissure angle, with the increase in confining pressure, the fissure aperture thickness of granite specimen also decreases a lot expect for the difference of crack system mode.

Table 5 Initiated crack types of granite specimens containing a single fissure under conventional triaxial compression

Fissure geometry	σ_3 /MPa	T_w	T_s	T_a	T_{as}	S_s	S_m	S_a	F_t	F_s
$\alpha = 0^\circ$	0	✓	✓							
	5	✓							✓	
	10	✓		✓	✓				✓	
	20							✓		
$\alpha = 30^\circ$	0	✓	✓						✓	
	5	✓	✓	✓					✓	
	10	✓	✓						✓	
	20							✓	✓	
$\alpha = 45^\circ$	0	✓	✓							
	5	✓				✓	✓			
	10			✓					✓	✓
	20						✓			
$\alpha = 60^\circ$	0	✓	✓						✓	
	5			✓					✓	✓
	10	✓		✓					✓	✓
	20			✓				✓	✓	✓
$\alpha = 90^\circ$	0	✓		✓					✓	✓
	5	✓	✓						✓	✓
	10	✓							✓	✓
	20	✓					✓			✓

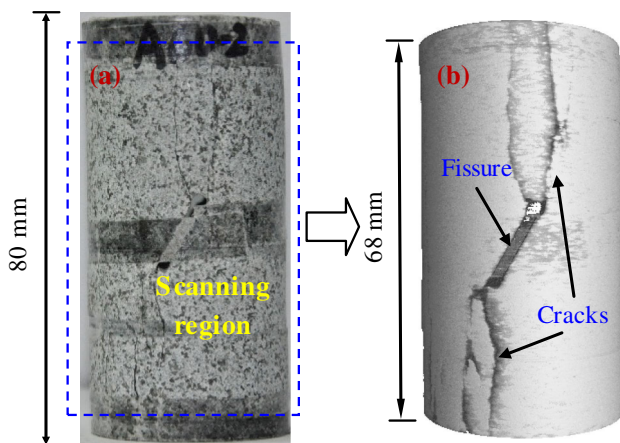


Fig. 20 Illustration of scanning region of X-ray microCT observation. **a** Experimental specimen; **b** CT image

Conclusions

Conventional triaxial compression experiments were performed to investigate the strength, deformability and failure behavior of granite containing a single fissure. On the basis of the experimental results in this research, the following conclusion can be obtained.

1. Compared to an intact specimen, granite specimens containing a single fissure fail with lower peak strengths and crack damage thresholds and smaller elastic moduli and failure axial strains. The stress–

strain curve of fissured specimens shows an abrupt change of slope under various confining pressures, coincident with the propagation of tensile and shear cracks at the upper and lower fissure tips. The peak axial strain of an intact granite specimen increases linearly with increasing confining pressure. However, for specimens containing a single fissure, the failure axial strain usually ranges from 0.20 to 7.86% and increases nonlinearly with increasing σ_3 for the same angle of the single fissure. The failure axial strain is significantly influenced by crack propagation in specimens containing a single fissure under different confining pressures.

2. The influence of the confining pressure on the crack damage threshold and the peak strength of granite with respect to various fissure angles is evaluated. For the same fissure angle, the crack damage threshold and the peak strength of granite both increase with the confining pressure, which is in good agreement with linear Mohr–Coulomb criterion. With the increase in the fissure angle, the cohesion of granite first increases and later decreases, but the internal friction angle is not obviously dependent to the fissure angle. The cohesion of granite containing a single fissure obtained by the crack damage threshold is lower than that obtained by the peak strength, but the internal friction angle of granite containing a single fissure obtained by the crack damage threshold is approximately equal to that obtained by the peak strength.

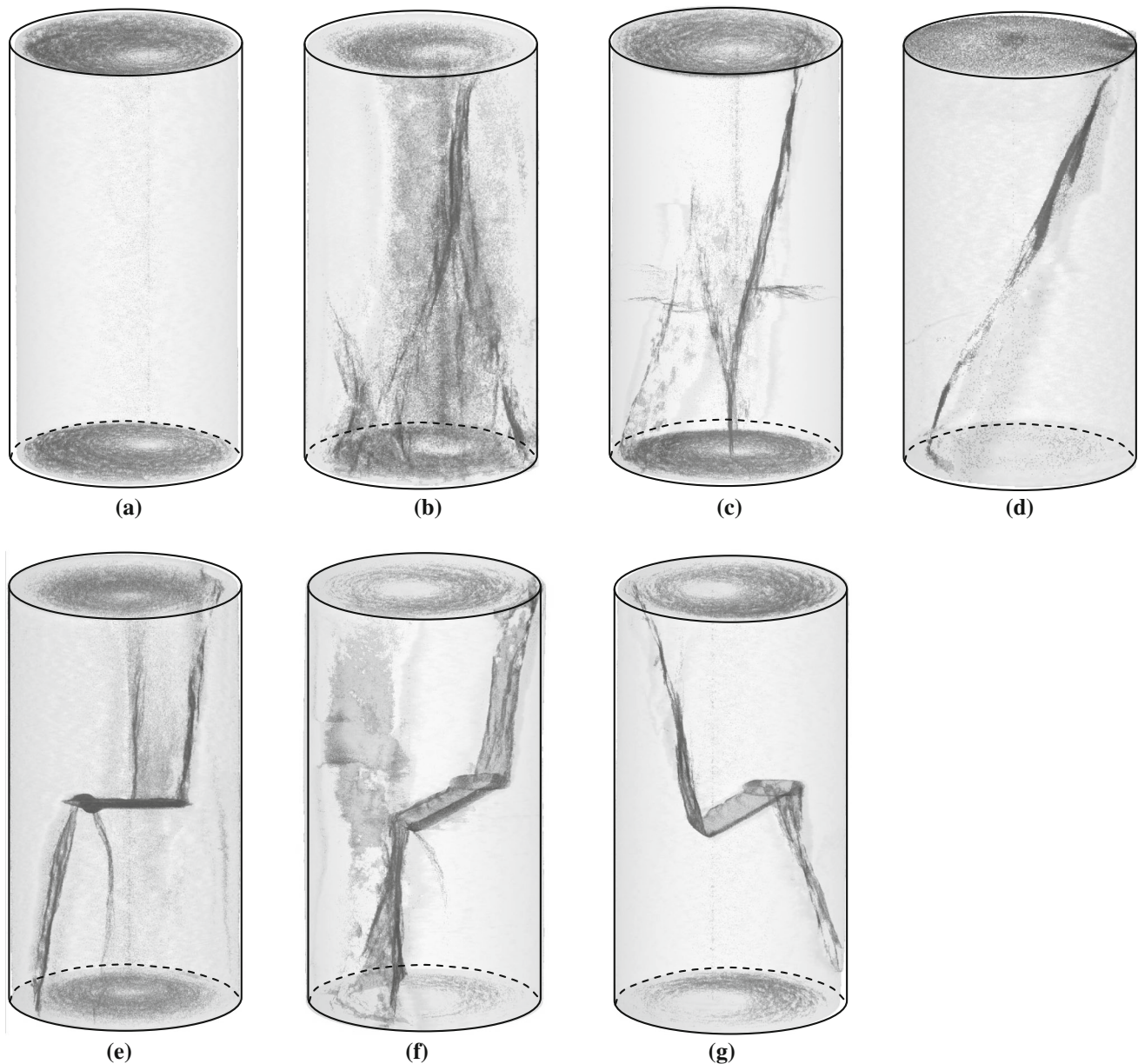


Fig. 21 3-D CT images of intact and fissured granite specimen containing a single fissure after uniaxial and triaxial compression. **a** Uncompressed intact specimen. **b** Intact specimen $\sigma_3 = 0$ MPa.

c Intact specimen $\sigma_3 = 10$ MPa. **d** Intact specimen $\sigma_3 = 30$ MPa. **e** $\alpha = 0^\circ$; $\sigma_3 = 0$ MPa. **f** $\alpha = 30^\circ$; $\sigma_3 = 0$ MPa. **g** $\alpha = 30^\circ$; $\sigma_3 = 20$ MPa

3. Nine different crack types are identified based on their geometry and crack propagation mechanism (tensile, shear and far-field crack) by analyzing the ultimate failure modes of granite specimens containing a single fissure under different confining pressures. Among the nine crack types, four of them (crack types T_w , T_s , T_a and T_{as}) are tensile, three of them (crack types S_m , S_s and S_a) are shear crack, and two of them (crack types F_t and F_s) are far-field. Tensile cracks T_w and T_s are easier to initiate for lower confining pressure (0–10 MPa), but for $\alpha = 90^\circ$, the tensile wing cracks

T_w are observed in all of the specimens. Shear cracks S_a and S_m are usually easier to initiate and nucleate for larger confining pressures, e.g., when the confining pressure is 20 MPa. However, for $\sigma_3 = 5$ MPa, only the specimen for $\alpha = 45^\circ$ initiates shear cracks S_m and S_s , and the specimen for $\alpha = 30^\circ$ initiates shear cracks S_a .

4. A series of X-ray microcomputed tomography (CT) observations were conducted to analyze the internal damage mechanism of the granite specimens with respect to various fissure angles. Reconstructed 3-D

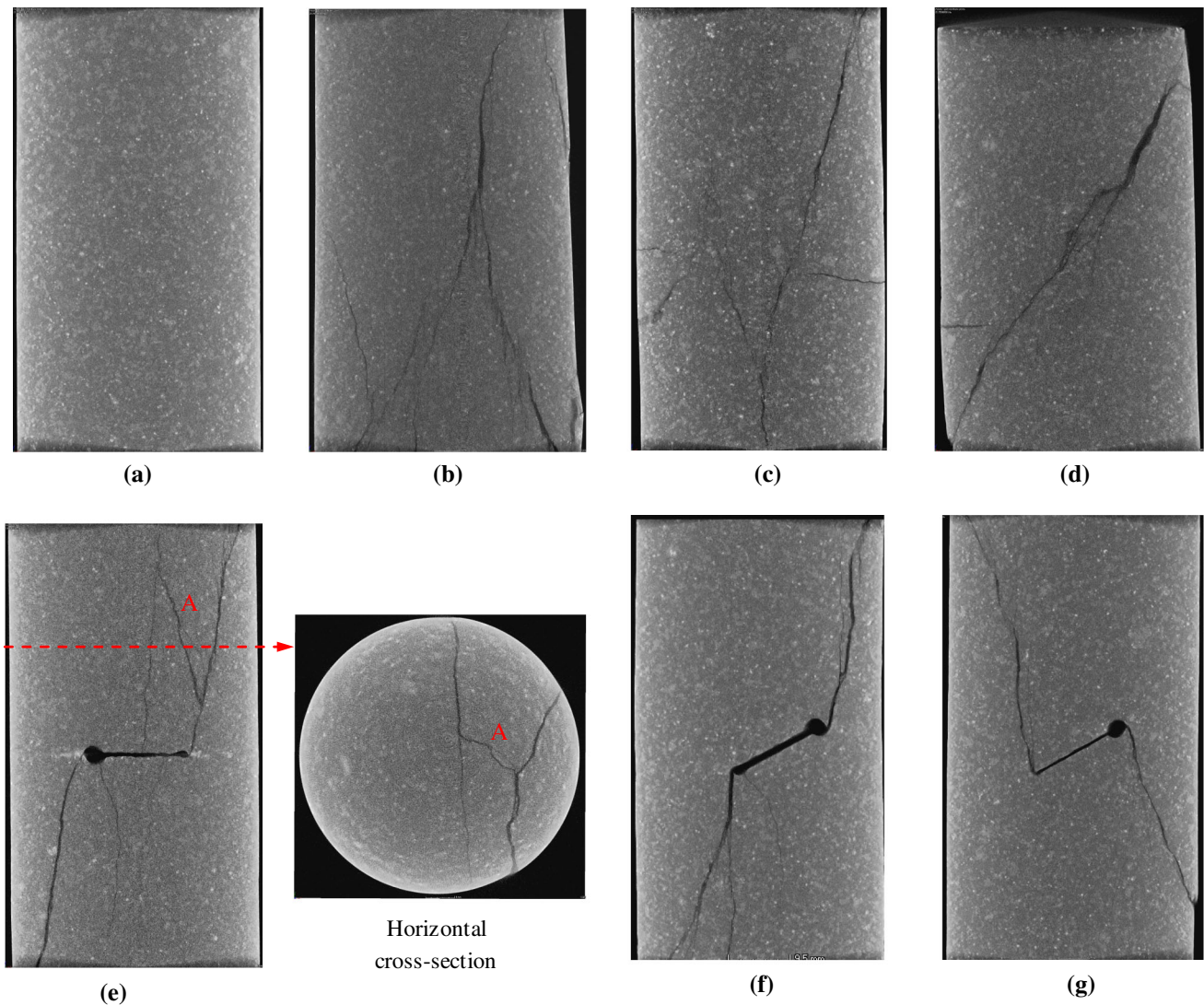


Fig. 22 Internal vertical CT cross sections of intact and fissured granite specimen containing a single fissure after uniaxial and triaxial compression. **a** Uncompressed intact specimen. **b** Intact specimen

$\sigma_3 = 0$ MPa. **c** Intact specimen $\sigma_3 = 10$ MPa. **d** Intact specimen $\sigma_3 = 30$ MPa. **e** $\alpha = 0^\circ$; $\sigma_3 = 0$ MPa. **f** $\alpha = 30^\circ$; $\sigma_3 = 0$ MPa. **g** $\alpha = 30^\circ$; $\sigma_3 = 20$ MPa

CT images indicate obvious effects of the confining pressure and the fissure angle on the crack system of granite specimens. The initiated position of the first cracks transfers from the middle position to the fissure tip. For the same fissure angle, with increasing confining pressure, the tensile wing and secondary tensile cracks are restricted; the anti-tensile, main shear crack and anti-shear crack dominate the ultimate failure mode of granite specimens.

Acknowledgements This research was supported by the Fundamental Research Funds for the Central Universities (2015XKZD05). We would also like to acknowledge the editor and the anonymous reviewers for their valuable comments, which have greatly improved this paper.

References

Chen L, Liu JF, Wang CP, Liu J, Su R, Wang J (2014) Characterization of damage evolution in granite under compressive stress condition and its effect on permeability. *Int J Rock Mech Min Sci* 71:340–349

Fairhurst CE, Hudson JA (1999) Draft ISRM suggested method for the complete stress–strain curve for the intact rock in uniaxial compression. *Int J Rock Mech Min Sci* 36(3):279–289

Fan QX, Zhu HB, Geng J (2015) Monitoring result analysis of high slope of five-step ship lock in the Three Gorges Project. *J Rock Mech Geotech Eng* 7:199–206

Fujii Y, Ishijima Y (2004) Consideration of fracture growth from an inclined slit and inclined initial fracture at the surface of rock and mortar in compression. *Int J Rock Mech Min Sci* 41:1035–1041

Heap MJ, Baud P, Meredith PG, Bell AF, Main IG (2009) Time-dependent brittle creep in Darley Dale sandstone. *J Geophys Res.* doi:10.1029/2008JB006212

- Jia L, Chen M, Zhang W, Xu T, Zhou Y, Hou B, Jin Y (2013) Experimental study and numerical modeling of brittle fracture of carbonate rock under uniaxial compression. *Mech Res Commun* 50(4):58–62
- Lee H, Jeon S (2011) An experimental and numerical study of fracture coalescence in pre-cracked specimens under uniaxial compression. *Int J Solids Struct* 48(6):979–999
- Li YP, Chen LZ, Wang YH (2005) Experimental research on pre-cracked marble under compression. *Int J Solids Struct* 42(9/10):2505–2516
- Lu ZD, Ding WX, Feng XT, Zhang YL (2008) Experimental study on mechanical-hydraulic-chemical coupling process in cracked rocks. *Chin J Rock Mech Eng* 27(4):796–804 (in Chinese)
- Lu Y, Wang L, Elsworth D (2015) Uniaxial strength and failure in sandstone containing a pre-existing 3-D surface flaw. *Int J Fract* 194(1):59–79
- Park CH, Bobet A (2009) Crack coalescence in specimens with open and closed flaws: a comparison. *Int J Rock Mech Min Sci* 46(5):819–829
- Prudencio M, Van Sint Jan M (2007) Strength and failure modes of rock mass models with non-persistent joints. *Int J Rock Mech Min Sci* 44(6):890–902
- Shi AC (2006) Study on performance and method of feedback design in high rock slope engineering. Hohai University, Nanjing
- Sun Q, Zhang W, Xue L, Zhang Z, Su T (2015) Thermal damage pattern and thresholds of granite. *Environ Earth Sci* 74(3):2341–2349
- Wang Y, Li X, Wu YF, Lin C, Zhang B (2015) Experimental study on meso-damage cracking characteristics of RSA by CT test. *Environ Earth Sci* 73(9):5545–5558
- Wong RHC, Chau KT (1998) Crack coalescence in a rock-like material containing two cracks. *Int J Rock Mech Min Sci* 35(2):147–164
- Wong LNY, Einstein HH (2009) Systematic evaluation of cracking behavior in specimens containing single flaws under uniaxial compression. *Int J Rock Mech Min Sci* 46(2):239–249
- Wong TF, David C, Zhu W (1997) The transition from brittle faulting to cataclastic flow in porous sandstones. *Mech Deformat J Geophys Res* 102(B2):3009–3025
- Yang SQ, Jing HW (2011) Strength failure and crack coalescence behavior of brittle sandstone samples containing a single fissure under uniaxial compression. *Int J Fract* 168(2):227–250
- Yang SQ, Jiang YZ, Xu WY, Chen XQ (2008) Experimental investigation on strength and failure behavior of pre-cracked marble under conventional triaxial compression. *Int J Solids Struct* 45(17):4796–4819
- Yang SQ, Yang DS, Jing HW, Li YH, Wang SY (2012a) An experimental study of the fracture coalescence behaviour of brittle sandstone specimens containing three fissures. *Rock Mech Rock Eng* 45(4):563–582
- Yang SQ, Jing HW, Wang SY (2012b) Experimental investigation on the strength, deformability, failure behavior and acoustic emission locations of red sandstone under triaxial compression. *Rock Mech Rock Eng* 45(4):583–606
- Yang Y, Ju Y, Sun Y, Zhang D (2015) Numerical study of the stress field during crack growth in porous rocks. *Geomech Geophys Geo-Energy Geo-Resour* 1(3):91–101
- Yang SQ, Ranjith PG, Jing HW, Tian WL, Ju Y (2017) An experimental investigation on thermal damage and failure mechanical behavior of granite after exposure to different high temperature treatments. *Geothermics* 65:180–197
- Yu Y, Yin JM (2004) Energy dissipation properties of three gorges granite under different loading modes. *Chin J Rock Mech Eng* 23(2):205–208 (in Chinese)
- Zhang XP, Wong LNY (2012) Cracking processes in rock-like material containing a single flaw under uniaxial compression: a numerical study based on parallel bonded-particle model approach. *Rock Mech Rock Eng* 45:711–737
- Zhao XG, Cai M, Wang J, Ma LK (2013) Damage stress and acoustic emission characteristics of the Beishan granite. *Int J Rock Mech Min Sci* 64:258–269
- Zhao GF, Russell AR, Zhao X, Khalili N (2014) Strain rate dependency of uniaxial tensile strength in gosford sandstone by the distinct lattice spring model with x-ray micro CT. *Int J Solids Struct* 51:1587–1600
- Zhao YS, Wan ZJ, Feng ZJ, Xu ZH, Liang WG (2017) Evolution of mechanical properties of granite at high temperature and high pressure. DOI, *Geomech Geophys Geo-Energy Geo-Resour*. doi:10.1007/s40948-017-0052-8
- Zhu ZQ, Sheng Q, Leng XL, Zhang ZR (2007) Study on crack initiation mechanism of three gorges granite. *Chin J Rock Mech Eng* 26(12):2570–2575 (in Chinese)